Dynamic Behaviors of Couple Stress Quadrilateral Thick Microplates within a Refined DQFE Framework

Zihao Peng[a], Bo Zhang[a, *], Mohamed Jebahi[b], Pengjun Wen[a], Cheng Li[c], Xu Zhang[a]

[a]*Applied Mechanics and Structure Safety Key Laboratory of Sichuan Province, School of Mechanics and Aerospace Engineering, Southwest Jiaotong University, Chengdu, 61756, China*

[b]*Arts et Metiers Institute of Technology, CNRS, Université de Lorraine, LEM3, F-57000 Metz, France*

[c]*School of Automotive Engineering, Changzhou Institute of Technology, Jiangsu, Changzhou 213000, China*

Abstract: This study proposes a novel refined differential quadrature finite element (DQFE) framework for the size-dependent dynamic analysis of thick quadrilateral microplates, incorporating couple-stress effect and two kinematic variables. The proposed methodology addresses inter-element compatibility through fifth-order differential quadrature geometric mapping while achieving geometric adaptability via global-local coordinate transformation. Detailed procedures for assembling element matrices and imposing boundary conditions are provided. Validation through representative quadrilateral plate configurations confirms the efficacy of the proposed framework, with particular success in modeling asymmetric trapezoidal plates through experimental correlation. The enhanced DQFE framework further elucidates fundamental mechanisms governing cyclic quadrilateral microplate dynamics by systematically investigating three critical factors: material length scale parameters (MLSP), thickness-to-length ratios, and boundary constraint configurations. Mode localization characteristics are quantitatively assessed using the mode assurance criterion. The principal conclusions reveal: (1) Superior convergence characteristics of the fifty-degree-of-freedom DQFE formulation compared to conventional lower-order implementations; (2) Emergence of mode-transition phenomena driven by central angle variations; (3) Differential sensitivity of critical mode-transition angles to MLSP variations under contrasting boundary constraint intensities; (4) Characteristic modification of vibration mode contours induced by size-dependent effects.

Keywords: Dynamic behaviors; Quadrilateral thick microplates; Couple stress; Differential quadrature finite element; Mode localization phenomenon.

1 Introduction

Recent advancements in ultra-precision manufacturing and semiconductor technologies have propelled the development of miniaturized devices for micro/nano-electromechanical systems (MEMS/NEMS) applications [1-6]. These micro/nanoscale architectures leverage inherent advantages over macroscale systems, particularly in spatial efficiency, mass reduction, cost performance, and operational stability. The dimensional transition from macro- to micro/nanoscale intensifies microstructure-dependent material responses, exposing limitations in classical continuum mechanics frameworks that disregard material length scale parameters (MLSPs) [7]. This recognition has stimulated the development of enhanced continuum frameworks encompassing nonlocal elasticity theory (NET) [8], surface elasticity theory (SET) [9], strain gradient theory [10, 11], modified couple stress theory (MCST) [12], modified strain gradient theory (MSGT) [13], and nonlocal strain gradient theory (NSGT) [14], which address size-dependent phenomena through distinct physical mechanisms.

In recent decades, non-classical continuum theories have been integrated with the assumption of classical plate theory (CPT), first-order shear deformation theory (FSDT), or higher-order shear deformation theory (HSDT) to predict the global mechanical behaviors of small-scale plates [15-27]. However, research on small-scale quadrilateral plates within HSDT frameworks remains scarce. While rectangular and skew microplates (as quadrilateral subsets) have been extensively studied, their generalized quadrilateral counterparts remain understudied despite their engineering significance. These structures, with their geometric versatility, play critical roles in aerospace, marine, civil engineering, and MEMS applications. The geometric diversity inherent in arbitrary quadrilateral configurations induces intricate vibrational

behaviors, making mode shape prediction more challenging than regular geometries. Although macroscale quadrilateral plates have been thoroughly examined through numerical methodologies [28-33], their microscale counterparts remain largely unexplored.

Recent research has systematically investigated microplate vibration and buckling phenomena through advanced nonclassical continuum mechanics approaches. J.N. Reddy et al. pioneered the integration of MCST into the analysis of microbeams and microplates. Their key advancements comprise: (i) Microstructure-dependent nonlinear formulations of Euler–Bernoulli and Timoshenko beam theories, incorporating through-thickness power-law gradients in two-constituent materials [34], (ii) a general third-order plate theory incorporating microstructure-dependent length scale parameters and von Kármán nonlinearity [35], and (iii) axisymmetric bending analyses of functionally graded (FG) circular plates by classical and first-order plate theories [36, 37]. Nguyen et al. [38] developed a size-dependent numerical HSDT composite microplate buckling method using MCST and isogeometric analysis (IGA). Le et al. analyzed porous metal foam microplates' linear and nonlinear responses with MCST and IGA [39] and proposed a nonlocal solution combining Carrera Unified Formulation and IGA for static and vibration analysis of laminated nanoplates [40]. Nguyen and Phan [41] studied the dynamic instability of CPT nanoplates via IGA. Malekzadeh et al. [42] examined the free vibration of orthotropic arbitrary straight-edged quadrilateral nanoplates employing NET and FSDT. Huang et al. [43] calibrated the size-dependent parameters of single-layer graphene sheets, modeled as simply supported rectangular plates using NET and Navier solution. Shenas and Malekzadeh [44] investigated the free vibration of FG quadrilateral microplates in thermal environments using MSGT and FSDT. Babu and Patel [45] employed Levy's method to study the static bending of rectangular nanoplates based on the CPT and strain gradient elasticity. Using sinusoidal shear deformation theory, Shokravi and Jalili [46] analyzed laminated quadrilateral microplates' thermal dynamic buckling behaviors of with NET. Zhang et al. [47] developed a four-node quadrilateral element with 48 DOF for strain gradient Mindlin microplates. Karamanli [48] analyzed the transient vibration of FG square microplates under a moving concentrated load using quasi-3D shear and normal deformation plate theory. Emdadi et al. [49] applied the differential quadrature method (DQM) to investigate the vibration of nanocomposite annular sandwich microplates, integrating MCST with HSDT. Mao et al. [50] explored the size-dependent static and dynamic behaviors of thin triangular CPT microplates based on the MCST with micro-inertia, while another study by Mao et al. [51] proposed a four-node nonconforming element for static and dynamic analyses of orthotropic thin microplates within the consistent couple stress theory (CCST). Nuhu and Safaei [52, 53] comprehensively reviewed nonclassical continuum modeling methodologies for microplates with diverse geometries and loading configurations.

The reviewed literature demonstrates that current investigations on microscale plates predominantly concentrate on analytical solutions for rectangular/annular geometries and numerical approaches for quadrilateral configurations using CPT or FSDT. The necessity of shear correction factors in FSDT to address discrepancies between theoretical and actual transverse shear distributions remains well acknowledged. While Reddy's HSDT achieves marginal accuracy improvement over FSDT, it introduces significant computational demands. Both frameworks necessitate three out-of-plane kinematic variables for plate deformation characterization. The refined HSDT [54] offers theoretical simplification through dual out-of-plane variables, enhancing quadrilateral microplate modeling efficiency. Current research exhibits notable limitations in predicting thick microplate vibration phenomena, specifically regarding size-effect-induced modal localization/transition mechanisms [55] involving shear deformation coupling. Although Niiranen et al. [56] identified gradient parameter influences on annular plate modal characteristics during free vibration analysis, their work omitted quantitative evaluation of parametric impact magnitudes on modal evolution.

This work undertakes a comprehensive theoretical-numerical evaluation of couple-stress quadrilateral thick microplate dynamics to address these research deficiencies. The research framework comprises: Section 2 establishes MCST-based free vibration modeling integrating refined HSDT for quadrilateral microplates. Section 3 formulates a 50-DOF nine-node DQFE scheme with global-local coordinate

transformation for quadrilateral domain adaptability, implementing boundary constraints via singular value decomposition. Section 4 verifies method convergence through comparative analysis with conventional four-node DQFE and validates accuracy through vibration frequency comparisons across rectangular, skewed, symmetric/asymmetric trapezoidal, and annular sectorial plates against benchmark solutions. Case analysis of cyclic quadrilateral plates elucidates MLSP and shear deformation impacts on frequency characteristics and modal localization patterns. Concluding remarks are presented in Section 5.

2 Theoretical modeling

2.1 Kinematics description and constitutive model

Fig. 1. illustrates an isotropic quadrilateral microplate with thickness h. The Cartesian reference frame $Oxyz$, employed for kinematic description, has its origin embedded within the mid-plane Oxy, with Oz normal to this plane. The displacement field follows the refined HSDT formulation [54], as mathematically expressed in Eq. (1):

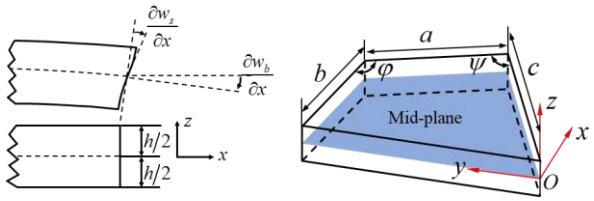

Fig. 1 Geometry of a quadrilateral microplate

$$u=-z\frac{\partial w_b}{\partial x}+\left(\frac{z}{4}-\frac{5z^3}{3h^2}\right)\frac{\partial w_s}{\partial x},\ v=-z\frac{\partial w_b}{\partial y}+\left(\frac{z}{4}-\frac{5z^3}{3h^2}\right)\frac{\partial w_s}{\partial y},\ w=w_b+w_s \tag{1}$$

where u, v, and w denote the displacement components along the x-, y-, and z-axes of the displacement field, respectively; w_b and w_s correspond to the bending and shear components of transverse displacement. Given the exclusive focus on out-of-plane vibration, the in-plane displacement components u_0 and v_0 are analytically omitted. When incorporating in-plane terms, the governing equations for w_b and w_s maintain independence from these displacement variables.

The modified couple stress theory, proposed by Yang [12], incorporates an additional higher-order equilibrium to govern couple stress behavior, rendering the couple stress tensor symmetric. This theory relies on a single material length scale parameter. For an isotropic linear elastic microstructure, the strain energy is expressed as follows:

$$U=\frac{1}{2}\int_{\Omega}\left(\sigma_{ij}\varepsilon_{ij}+m_{ij}\chi_{ij}\right)\mathrm{d}\Omega \tag{2}$$

In Eq. (2), σ_{ij}, ε_{ij}, m_{ij}, and χ_{ij} represent the stress tensor, strain tensor, symmetric part of the couple stress tensor, and symmetric part of the curvature tensor, respectively. These components are defined as follows:

$$\varepsilon_{ij}=\frac{1}{2}\left(u_{i,j}+u_{j,i}\right),\ \chi_{ij}=\frac{1}{2}\left(\theta_{i,j}+\theta_{j,i}\right),\ \theta_i=\frac{1}{2}e_{ijk}u_{k,j} \tag{3a}$$

$$\sigma_{ij}=\lambda\varepsilon_{kk}\delta_{ij}+2\mu\varepsilon_{ij},\ m_{ij}=2\mu l^2\chi_{ij} \tag{3b}$$

where a subscript comma followed by j denotes the partial derivatives with respect to x_j, where u_1, u_2, u_3 correspond to u, v, w, and x_1, x_2, x_3 correspond to x, y, z, respectively; θ_i denotes the component of the rotation vector; χ_{ij} is the gradient of the rotation vector; δ_{ij} represents the Kronecker delta; e_{ijk} denotes the Levi-Civita symbol; λ and μ are the Lamé constants of isotropic materials.

Placing Eq. (1) into Eq. (3a) gives the strain and curvature components as follows:

$$\begin{cases}\varepsilon_{xx}=-z\dfrac{\partial^2 w_b}{\partial x^2}+\left(\dfrac{z}{4}-\dfrac{5z^3}{3h^2}\right)\dfrac{\partial^2 w_s}{\partial x^2},\ \varepsilon_{yy}=-z\dfrac{\partial^2 w_b}{\partial y^2}+\left(\dfrac{z}{4}-\dfrac{5z^3}{3h^2}\right)\dfrac{\partial^2 w_s}{\partial y^2},\ \varepsilon_{zz}=0,\\ \varepsilon_{xy}=-z\dfrac{\partial^2 w_b}{\partial x\partial y}+\left(\dfrac{z}{4}-\dfrac{5z^3}{3h^2}\right)\dfrac{\partial^2 w_s}{\partial x\partial y},\ \varepsilon_{xz}=\left(\dfrac{5}{8}-\dfrac{5z^2}{2h^2}\right)\dfrac{\partial w_s}{\partial x},\ \varepsilon_{yz}=\left(\dfrac{5}{8}-\dfrac{5z^2}{2h^2}\right)\dfrac{\partial w_s}{\partial y},\end{cases} \tag{4a}$$

$$\begin{cases} \chi_{xx}=\left(\frac{3}{8}+\frac{5z^2}{2h^2}\right)\frac{\partial^2 w_s}{\partial x\partial y}+\frac{\partial^2 w_b}{\partial x\partial y}, \chi_{yy}=-\left(\frac{3}{8}+\frac{5z^2}{2h^2}\right)\frac{\partial^2 w_s}{\partial x\partial y}-\frac{\partial^2 w_b}{\partial x\partial y}, \chi_{zz}=0, \\ \chi_{xy}=\left(\frac{3}{16}+\frac{5z^2}{4h^2}\right)\left(\frac{\partial^2 w_s}{\partial y^2}-\frac{\partial^2 w_s}{\partial x^2}\right)+\frac{1}{2}\left(\frac{\partial^2 w_b}{\partial y^2}-\frac{\partial^2 w_b}{\partial x^2}\right), \chi_{yz}=-\frac{5z}{2h^2}\frac{\partial w_s}{\partial x}, \chi_{xz}=\frac{5z}{2h^2}\frac{\partial w_s}{\partial y} \end{cases} \tag{4b}$$

The stress and couple stress components are obtained by substituting Eqs. (4a) and (4b) into Eq. (3b).

2.2 Governing equation

Based on Eq. (1), the kinetic energy is derived as follows:

$$\Pi_k=\int_A\left\{\frac{\rho h^3}{24}\left[\left(\frac{\partial \dot{w}_b}{\partial x}\right)^2+\left(\frac{\partial \dot{w}_b}{\partial y}\right)^2\right]+\frac{\rho h}{2}\left(\dot{w}_b+\dot{w}_s\right)^2+\frac{\rho h^3}{2016}\left[\left(\frac{\partial \dot{w}_s}{\partial x}\right)^2+\left(\frac{\partial \dot{w}_s}{\partial y}\right)^2\right]\right\}\mathrm{d}A \tag{5}$$

where dot-superscript represents the time derivative of the transverse displacement w.

Using Eqs. (2)-(4b), the strain energy in the global coordinate system is expressed as follows:

$$\Pi_s=\int_A\left\{\begin{array}{l} \Sigma_1\left[\left(\frac{\partial^2 w_b}{\partial x^2}\right)^2+\left(\frac{\partial^2 w_b}{\partial y^2}\right)^2\right]+\Sigma_2\left[\left(\frac{\partial^2 w_s}{\partial x^2}\right)^2+\left(\frac{\partial^2 w_s}{\partial y^2}\right)^2\right]+\left(\Sigma_3-\Sigma_6\right)\frac{\partial^2 w_b}{\partial x^2}\frac{\partial^2 w_b}{\partial y^2}+ \\ \left(\frac{\Sigma_3}{84}-\frac{3\Sigma_6}{8}\right)\frac{\partial^2 w_s}{\partial x^2}\frac{\partial^2 w_s}{\partial y^2}+\Sigma_4\left[\left(\frac{\partial w_s}{\partial x}\right)^2+\left(\frac{\partial w_s}{\partial y}\right)^2\right]+\Sigma_5\left[\left(\frac{\partial^2 w_s}{\partial x\partial y}\right)^2+84\left(\frac{\partial^2 w_b}{\partial x\partial y}\right)^2\right]+ \\ \frac{7\Sigma_6}{12}\left(\frac{\partial^2 w_b}{\partial x^2}-\frac{\partial^2 w_b}{\partial y^2}\right)\left(\frac{\partial^2 w_s}{\partial x^2}-\frac{\partial^2 w_s}{\partial y^2}\right)+\frac{7\Sigma_6}{3}\frac{\partial^2 w_b}{\partial x\partial y}\frac{\partial^2 w_s}{\partial x\partial y}+2\Sigma_6\left(\frac{\partial^2 w_b}{\partial x\partial y}\right)^2+\frac{3\Sigma_6}{4}\left(\frac{\partial^2 w_s}{\partial x\partial y}\right)^2 \end{array}\right\}\mathrm{d}A \tag{6}$$

where the coefficients Σ_1, Σ_2, Σ_3, Σ_4, Σ_5 and Σ_6 are

$$\begin{cases} \Sigma_1=\frac{D}{2}+\frac{\mu h l^2}{2}, \Sigma_2=\frac{D}{168}+\frac{3\mu h l^2}{16}, \Sigma_3=D\nu \\ \Sigma_4=\frac{5\mu h}{12}+\frac{25\mu l^2}{24h}, \Sigma_5=\frac{\mu h^3}{504}, \Sigma_6=\mu h l^2, D=\frac{Eh^3}{12\left(1-\nu^2\right)} \end{cases} \tag{7}$$

From Eqs. (5) and (6), the Euler-Lagrange equations for the microplate are formulated as follows:

$$\delta w_b: 2\Sigma_1\nabla^4 w_b+\frac{7\Sigma_6}{12}\nabla^4 w_s=\frac{\rho h^3}{12}\left(\frac{\partial^4 \ddot{w}_b}{\partial x^2\partial t^2}+\frac{\partial^4 \ddot{w}_b}{\partial y^2\partial t^2}\right)-\rho h\frac{\partial^2\left(\ddot{w}_b+\ddot{w}_s\right)}{\partial t^2} \tag{8a}$$

$$\delta w_s: \frac{7\Sigma_6}{12}\nabla^4 w_b+2\Sigma_5\frac{\partial^4 w_s}{\partial x^2\partial y^2}+2\Sigma_2\nabla^4 w_s-2\Sigma_4\nabla^2 w_s=\frac{\rho h^3}{1008}\frac{\partial^2\left(\nabla^2 \ddot{w}_s\right)}{\partial t^2}-\rho h\frac{\partial^2\left(\ddot{w}_b+\ddot{w}_s\right)}{\partial t^2} \tag{8b}$$

where $\Sigma_1=\frac{\Sigma_3}{2}+42\Sigma_5+\frac{\Sigma_6}{2}$ and $\Sigma_2=\frac{\Sigma_3}{168}+\frac{3\Sigma_6}{16}$ are satisfied.

By combining these equations, a governing equation incorporating both bending and shear effects is obtained:

$$\begin{array}{l} \left(4\Sigma_1\Sigma_2-\frac{49\Sigma_6^2}{144}\right)\nabla^8 w_b+4\Sigma_1\Sigma_5\frac{\partial^4\nabla^4 w_b}{\partial x^2\partial y^2}+4\Sigma_1\Sigma_4\nabla^6 w_b+\frac{h^6\rho^2}{12096}\frac{\partial^4\nabla^4 w_b}{\partial t^4}+\frac{85h^4\rho^2}{1008}\frac{\partial^4\nabla^2 w_b}{\partial t^4} \\ -\frac{\rho h^3\Sigma_5}{6}\frac{\partial^6\nabla^2 w_b}{\partial t^2\partial x^2\partial y^2}-\frac{\rho h\left(h^2\Sigma_4+12\Sigma_1+12\Sigma_2-7\Sigma_6\right)}{6}\frac{\partial^2\nabla^4 w_b}{\partial t^2}-2\rho h\Sigma_4\frac{\partial^2\nabla^2 w_b}{\partial t^2} \\ -\frac{\rho h^3\left(\Sigma_1+84\Sigma_2\right)}{504}\frac{\partial^2\nabla^6 w_b}{\partial t^2}-2\rho h\Sigma_5\frac{\partial^6 w_b}{\partial t^2\partial x^2\partial y^2}=0 \end{array} \tag{9}$$

where w_b can be substituted with w_s and ∇^2 is the Laplacian operator.

For CPT plates, the governing equation is a fourth-order partial differential equation. In contrast, the inclusion of couple stress and shear deformation effects in the present non-classical model increases the order to eight. Neglecting these factors, Eq. (9) can be reduced to the governing equation for CPT plates. Analytical solutions for general boundary conditions are challenging to derive, particularly for boundary conditions beyond simply supported edges. A numerical solution scheme is required to address this issue.

3 Numerical solution scheme

Introducing curvature tensor considerably increases the order of partial differential equations for small-scale plates compared to the classical plate models. This higher-order complexity and additional boundary conditions present substantial challenges in solving the associated boundary value problems. To address these challenges, researchers have developed various size-dependent numerical methods, including standard FEM [57, 58], mixed FEM [59], finite layer method [60], boundary element method [61], meshless methods [62-64], neural network-based methods [65], DQM [66], generalized conforming Trefftz elements [67], penalty hexahedral element for flexoelectric solids [68] and the peri-dynamic differential operator (PDDO) method [69]. Recently, Zhang's group [70-75] developed a series of DQFEs for rectangular microplates, incorporating couple-stress/strain-gradient effects. A notable characteristic of DQFE-based methods is the unification of quadrature points and element nodes, which uniquely integrates numerical calculations directly into the potential functional during element construction. However, previous studies on DQFEs have primarily focused on simple four-node configurations, excluding mid-edge and central nodes.

3.1 Coordinate transformation

The quadrilateral domain in the global coordinate system should be mapped onto an isoparametric coordinate system so that the integral can be operated. Similarly, Fan et al. [76] use a four-node isoparametric mapping in the numerical manifold method and Shang et al. [77] developed a four-node quadrilateral FSDT Trefftz-unsymmetric FEM. This study proposes a fifth-order Gauss-Lobatto DQ geometric mapping scheme for discretization and dimensionality-reduction, as illustrated in Fig. 2. This mapping approach extends the four-node DQFE framework discussed in earlier studies [47].

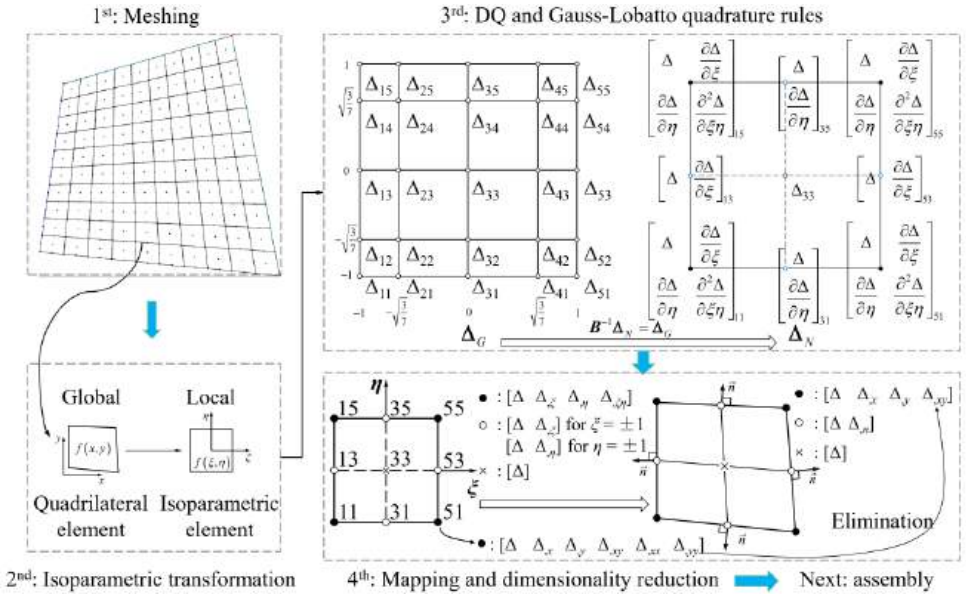

Fig. 2 Fifth-order differential quadrature geometric mapping scheme

The shape functions for the nine-node isoparametric element are expressed as follows:

$$\begin{aligned} N_i = &\left(1+\xi\xi_i\right)\left(1+\eta\eta_i\right)\xi\xi_i\eta\eta_i/4+\left(1-\xi^2\right)\left(1+\eta\eta_i\right)\left(1-\xi_i^2\right)\eta\eta_i/2+ \\ &\left(1-\eta^2\right)\left(1+\xi\xi_i\right)\left(1-\eta_i\right)\xi\xi_i/2+\left(1-\xi^2\right)\left(1-\eta^2\right)\left(1-\xi_i^2\right)\left(1-\eta_i^2\right) \end{aligned} \tag{10}$$

The 1st-order derivatives are obtained by chain rule: $(\,)_{,\xi}=(\,)_{,x}x_{,\xi}+(\,)_{,y}y_{,\xi}$ and $(\,)_{,\eta}=(\,)_{,x}x_{,\eta}+(\,)_{,y}y_{,\eta}$. The transformation for 2nd-order derivatives between global and local coordinate systems is given as follows:

$$\begin{Bmatrix} \dfrac{\partial^2}{\partial\xi^2} \\ \dfrac{\partial^2}{\partial\eta^2} \\ \dfrac{\partial^2}{\partial\xi\partial\eta} \end{Bmatrix} = \begin{bmatrix} J_{11}^2 & J_{12}^2 & 2J_{11}J_{12} \\ J_{21}^2 & J_{22}^2 & 2J_{21}J_{22} \\ J_{11}J_{21} & J_{12}J_{22} & J_{11}J_{22}+J_{12}J_{21} \end{bmatrix} \begin{Bmatrix} \dfrac{\partial^2}{\partial x^2} \\ \dfrac{\partial^2}{\partial y^2} \\ \dfrac{\partial^2}{\partial x\partial y} \end{Bmatrix} + \begin{bmatrix} \dfrac{\partial^2 x}{\partial\xi^2} & \dfrac{\partial^2 y}{\partial\xi^2} \\ \dfrac{\partial^2 x}{\partial\eta^2} & \dfrac{\partial^2 y}{\partial\eta^2} \\ \dfrac{\partial^2 x}{\partial\xi\partial\eta} & \dfrac{\partial^2 y}{\partial\xi\partial\eta} \end{bmatrix} \begin{Bmatrix} \dfrac{\partial}{\partial x} \\ \dfrac{\partial}{\partial y} \end{Bmatrix}, \begin{cases} J_{11}=\dfrac{\partial x}{\partial\xi} & J_{12}=\dfrac{\partial y}{\partial\xi} \\ J_{21}=\dfrac{\partial x}{\partial\eta} & J_{22}=\dfrac{\partial y}{\partial\eta} \end{cases} \tag{11}$$

The inverse mapping corresponding to Eq. (11) is as follows:

$$\frac{\partial^2\xi}{\partial x^2}=-\frac{1}{|\boldsymbol{J}|^2}\left[J_{22}^2\left(x_{,\xi\xi}\xi_{,x}+y_{,\xi\xi}\xi_{,y}\right)+J_{12}^2\left(x_{,\eta\eta}\xi_{,x}+y_{,\eta\eta}\xi_{,y}\right)-2J_{12}J_{22}\left(x_{,\xi\eta}\xi_{,x}+y_{,\xi\eta}\xi_{,y}\right)\right]$$

$$\frac{\partial^2\xi}{\partial y^2}=-\frac{1}{|\boldsymbol{J}|^2}\left[J_{12}^2\left(x_{,\xi\xi}\xi_{,x}+y_{,\xi\xi}\xi_{,y}\right)+J_{11}^2\left(x_{,\eta\eta}\xi_{,x}+y_{,\eta\eta}\xi_{,y}\right)-2J_{11}J_{21}\left(x_{,\xi\eta}\xi_{,x}+y_{,\xi\eta}\xi_{,y}\right)\right] \tag{12a}$$

$$\frac{\partial^2\xi}{\partial x\partial y}=-\frac{1}{|\boldsymbol{J}|^2}\left[\begin{array}{l}-J_{21}J_{22}\left(x_{,\xi\xi}\xi_{,x}+y_{,\xi\xi}\xi_{,y}\right)-J_{11}J_{12}\left(x_{,\eta\eta}\xi_{,x}+y_{,\eta\eta}\xi_{,y}\right)\\+\left(J_{11}J_{22}+J_{12}J_{21}\right)\left(x_{,\xi\eta}\xi_{,x}+y_{,\xi\eta}\xi_{,y}\right)\end{array}\right]$$

$$\frac{\partial^2\eta}{\partial x^2}=-\frac{1}{|\boldsymbol{J}|^2}\left[J_{22}^2\left(x_{,\xi\xi}\eta_{,x}+y_{,\xi\xi}\eta_{,y}\right)+J_{12}^2\left(x_{,\eta\eta}\eta_{,x}+y_{,\eta\eta}\eta_{,y}\right)-2J_{12}J_{22}\left(x_{,\xi\eta}\eta_{,x}+y_{,\xi\eta}\eta_{,y}\right)\right]$$

$$\frac{\partial^2\eta}{\partial y^2}=-\frac{1}{|\boldsymbol{J}|^2}\left[J_{12}^2\left(x_{,\xi\xi}\eta_{,x}+y_{,\xi\xi}\eta_{,y}\right)+J_{11}^2\left(x_{,\eta\eta}\eta_{,x}+y_{,\eta\eta}\eta_{,y}\right)-2J_{11}J_{21}\left(x_{,\xi\eta}\eta_{,x}+y_{,\xi\eta}\eta_{,y}\right)\right] \tag{12b}$$

$$\frac{\partial^2\eta}{\partial x\partial y}=-\frac{1}{|\boldsymbol{J}|^2}\left[\begin{array}{l}-J_{21}J_{22}\left(x_{,\xi\xi}\eta_{,x}+y_{,\xi\xi}\eta_{,y}\right)-J_{11}J_{12}\left(x_{,\eta\eta}\eta_{,x}+y_{,\eta\eta}\eta_{,y}\right)\\+\left(J_{11}J_{22}+J_{12}J_{21}\right)\left(x_{,\xi\eta}\eta_{,x}+y_{,\xi\eta}\eta_{,y}\right)\end{array}\right]$$

Using this transformation, the expression for kinetic energy in the global coordinate system, as outlined in Eq. (5), is rewritten in the local coordinate system as follows:

$$\Pi_k=\int_{-1}^{1}\int_{-1}^{1}\left\{\begin{array}{l}\alpha_1\left(\frac{\partial\dot{w}_b}{\partial\eta}\right)^2+\alpha_2\left(\frac{\partial\dot{w}_b}{\partial\xi}\right)^2+\alpha_3\left(\frac{\partial\dot{w}_s}{\partial\eta}\right)^2+\alpha_4\left(\frac{\partial\dot{w}_s}{\partial\xi}\right)^2+\\ \alpha_5\frac{\partial\dot{w}_b}{\partial\eta}\frac{\partial\dot{w}_b}{\partial\xi}+\alpha_6\frac{\partial\dot{w}_s}{\partial\eta}\frac{\partial\dot{w}_s}{\partial\xi}+\alpha_7\dot{w}_b^2+\alpha_8\dot{w}_s^2+\alpha_9\dot{w}_b\dot{w}_s\end{array}\right\}|\boldsymbol{J}|\mathrm{d}\xi\mathrm{d}\eta \tag{13}$$

The nine coefficients $\alpha_1 \sim \alpha_9$ are defined in Eq. (14):

$$\left\{\begin{array}{l}\alpha_1=\frac{\rho h^3}{24}\left[\left(\frac{\partial\eta}{\partial x}\right)^2+\left(\frac{\partial\eta}{\partial y}\right)^2\right],\ \alpha_2=\frac{\rho h^3}{24}\left[\left(\frac{\partial\xi}{\partial x}\right)^2+\left(\frac{\partial\xi}{\partial y}\right)^2\right],\ \alpha_3=\frac{\rho h^3}{2016}\left[\left(\frac{\partial\eta}{\partial x}\right)^2+\left(\frac{\partial\eta}{\partial y}\right)^2\right],\\ \alpha_4=\frac{\rho h^3}{2016}\left[\left(\frac{\partial\xi}{\partial x}\right)^2+\left(\frac{\partial\xi}{\partial y}\right)^2\right],\ \alpha_5=\frac{\rho h^3}{12}\left(\frac{\partial\xi}{\partial x}\frac{\partial\eta}{\partial x}+\frac{\partial\xi}{\partial y}\frac{\partial\eta}{\partial y}\right),\ \alpha_6=\frac{\rho h^3}{1008}\left(\frac{\partial\xi}{\partial x}\frac{\partial\eta}{\partial x}+\frac{\partial\xi}{\partial y}\frac{\partial\eta}{\partial y}\right),\\ \alpha_7=\frac{\rho h}{2},\ \alpha_8=\frac{\rho h}{2},\ \alpha_9=\rho h\end{array}\right. \tag{14}$$

Similarly, the strain energy derivatives with respect to global coordinates (x, y) in Eq. (6) are transformed into their counterparts in local coordinates (ξ, η). The resulting strain energy expression in the natural coordinate system is as follows:

$$\begin{aligned}\Pi_S=\int_{-1}^{1}\int_{-1}^{1}\big(&\beta_1 w_{s,\xi\eta}w_{b,\eta\eta}+\beta_2 w_{s,\xi\eta}w_{b,\xi\eta}+\beta_3 w_{s,\xi\eta}w_{b,\xi\xi}+\beta_5 w_{s,\xi\xi}w_{b,\eta\eta}+\beta_6 w_{s,\xi\xi}w_{b,\xi\eta}+\\&\beta_7 w_{s,\xi\xi}w_{b,\xi\xi}+\beta_{18}w_{s,\eta\eta}w_{b,\eta\eta}+\beta_{19}w_{s,\eta\eta}w_{b,\xi\eta}+\beta_{20}w_{s,\eta\eta}w_{b,\xi\xi}+\beta_{23}w_{s,\eta}w_{b,\eta\eta}+\\&\beta_{24}w_{s,\eta}w_{b,\xi\eta}+\beta_{25}w_{s,\eta}w_{b,\xi\xi}+\beta_{26}w_{s,\xi}w_{b,\eta\eta}+\beta_{27}w_{s,\xi}w_{b,\xi\eta}+\beta_{28}w_{s,\xi}w_{b,\xi\xi}+\\&\beta_{35}w_{s,\eta\eta}w_{b,\eta}+\beta_{36}w_{s,\eta\eta}w_{b,\xi}+\beta_{38}w_{s,\xi\eta}w_{b,\eta}+\beta_{39}w_{s,\xi\eta}w_{b,\xi}+\beta_{42}w_{s,\xi\xi}w_{b,\eta}+\\&\beta_{43}w_{s,\xi\xi}w_{b,\xi}+\beta_{51}w_{s,\eta}w_{b,\eta}+\beta_{52}w_{s,\eta}w_{b,\xi}+\beta_{53}w_{s,\xi}w_{b,\eta}+\beta_{54}w_{s,\xi}w_{b,\xi}+\\&\beta_4 w_{s,\xi\eta}w_{s,\eta\eta}+\beta_8 w_{s,\xi\xi}w_{s,\eta\eta}+\beta_9 w_{s,\xi\xi}w_{s,\xi\eta}+\beta_{13}w_{s,\eta\eta}^2+\beta_{14}w_{s,\xi\eta}^2+\beta_{15}w_{s,\xi\xi}^2+\\&\beta_{29}w_{s,\xi}w_{s,\eta\eta}+\beta_{37}w_{s,\eta\eta}w_{s,\eta}+\beta_{40}w_{s,\xi\eta}w_{s,\eta}+\beta_{41}w_{s,\xi\eta}w_{s,\xi}+\beta_{44}w_{s,\xi\xi}w_{s,\eta}+\\&\beta_{45}w_{s,\xi\xi}w_{s,\xi}+\beta_{48}w_{s,\eta}^2+\beta_{49}w_{s,\xi}^2+\beta_{55}w_{s,\xi}w_{s,\eta}+\beta_{10}w_{b,\eta\eta}^2+\beta_{11}w_{b,\xi\eta}^2+\beta_{12}w_{b,\xi\xi}^2+\\&\beta_{16}w_{b,\xi\xi}w_{b,\eta\eta}+\beta_{17}w_{b,\xi\xi}w_{b,\xi\eta}+\beta_{21}w_{b,\xi\eta}w_{b,\eta\eta}+\beta_{22}w_{b,\xi}w_{b,\eta\eta}+\beta_{30}w_{b,\eta\eta}w_{b,\eta}+\\&\beta_{31}w_{b,\xi\eta}w_{b,\eta}+\beta_{32}w_{b,\xi\eta}w_{b,\xi}+\beta_{33}w_{b,\xi\xi}w_{b,\eta}+\beta_{34}w_{b,\xi\xi}w_{b,\xi}+\beta_{46}w_{b,\eta}^2+\beta_{47}w_{b,\xi}^2+\\&\beta_{50}w_{b,\xi}w_{b,\eta}\big)|\boldsymbol{J}|\mathrm{d}\xi\mathrm{d}\eta\end{aligned} \tag{15}$$

In Eq. (15), the 55 coefficients from β_1 to β_{55} are functions of the coefficients (Σ_1, Σ_2..., Σ_6) given in Eq. (7) and the derivatives of the local coordinates (ξ, η) with respect to the global coordinates (x, y). The

detailed expressions for these coefficients are provided in Appendix A.

*3.2 **Discretization of potential energy functional***

The fifth-order Gauss-Lobatto quadrature rule defines the weighting coefficients and integration points in the two-dimensional standard domain $[-1, 1]\times[-1, 1]$ are given as $\xi=\eta=\left[-1, -\frac{\sqrt{21}}{7}, 0, \frac{\sqrt{21}}{7}, 1\right]$, and the weighting matrix $\boldsymbol{Q}$ is expressed as:

$$\boldsymbol{Q}=diag\begin{bmatrix} c_1^2, c_2c_1, c_3c_1, c_2c_1, c_1^2, c_2c_1, c_2^2, c_3c_2, c_2^2, c_2c_1, \\ c_3c_1, c_3c_2, c_3^2, c_3c_2, c_3c_1, c_2c_1, c_2^2, c_3c_2, c_2^2, c_2c_1, \\ c_1^2, c_2c_1, c_3c_1, c_2c_1, c_1^2 \end{bmatrix} where\ c_1=\frac{1}{10}, c_2=\frac{49}{90}, \text{ and } c_3=\frac{32}{45} \tag{16}$$

In Fig. 2, the deflection components of a quadrilateral microplate element at the quadrature points are expressed in the following column vector form:

$$\Delta_G=\begin{bmatrix}\Delta_{11} & \mathrm{K} & \Delta_{ij} & \mathrm{K} & \Delta_{55}\end{bmatrix}^{\mathrm{T}} \text{ with } ij=12:\ 51,\ 12:\ 52,\ 13:\ 53,\ 14:\ 54,\ 15:\ 54 \tag{17}$$

where Δ_{ij} represents w_s or w_b at the ij^{th} quadrature points.

The kinematic field and its differential derivatives are formulated via Lagrange interpolation utilizing quadrature point deflection values. Employing Lagrange polynomials as shape functions, this approach enables domain-wide transverse displacement representation as a weighted superposition of basis function:

$$\Delta(\xi,\eta)=\sum_{p=1}^{5}\sum_{q=1}^{5} l_{\xi p}(\xi)\cdot l_{\eta q}(\eta)\cdot\Delta_{pq} \tag{18}$$

where $l_{\xi p}$ and $l_{\eta q}$ are the Lagrange interpolation polynomials at the pth and qth quadrature points along the ξ and η directions, respectively, and Δ_{pq} represents the deflection component at the pqth quadrature point.

Using the DQ rule, the partial derivatives of the deflection variables are expressed as follows:

$$\left[\frac{\partial\Delta}{\partial\xi}\right]_G=\boldsymbol{A}_{\xi}\boldsymbol{\Delta}_G, \left[\frac{\partial\Delta}{\partial\eta}\right]_G=\boldsymbol{A}_{\eta}\boldsymbol{\Delta}_G, \left[\frac{\partial^2\Delta}{\partial\xi^2}\right]_G=\boldsymbol{A}_{\xi\xi}\boldsymbol{\Delta}_G, \left[\frac{\partial^2\Delta}{\partial\eta^2}\right]_G=\boldsymbol{A}_{\eta\eta}\boldsymbol{\Delta}_G, \left[\frac{\partial^2\Delta}{\partial\xi\partial\eta}\right]_G=\boldsymbol{A}_{\xi\eta}\boldsymbol{\Delta}_G \tag{19}$$

where the vectors are defined as follows:

$$\left[\frac{\partial^{p\oplus q}\Delta}{\partial\xi^p\partial\eta^q}\right]_G=\begin{bmatrix}\left\langle\frac{\partial^{p\oplus q}\Delta}{\partial\xi^p\partial\eta^q}\right\rangle_{11} & \mathrm{K} & \left\langle\frac{\partial^{p\oplus q}\Delta}{\partial\xi^p\partial\eta^q}\right\rangle_{ij} & \mathrm{K} & \left\langle\frac{\partial^{p\oplus q}\Delta}{\partial\xi^p\partial\eta^q}\right\rangle_{55}\end{bmatrix}^{\mathrm{T}} \tag{20}$$

$$\text{with } ij=12:\ 51,\ 12:\ 52,\ 13:\ 53,\ 14:\ 54,\ 15:\ 54$$

The five derivative matrices, $\boldsymbol{A}_{\xi}$, $\boldsymbol{A}_{\eta}$, $\boldsymbol{A}_{\xi\xi}$, $\boldsymbol{A}_{\eta\eta}$, and $\boldsymbol{A}_{\xi\eta}$, are defined under the DQ rule as follows:

$$\boldsymbol{A}_{\xi}=\begin{bmatrix}\boldsymbol{p}_{\xi} & \mathbf{0} & \mathbf{0} & \mathbf{0} & \mathbf{0}\\ \mathbf{0} & \boldsymbol{p}_{\xi} & \mathbf{0} & \mathbf{0} & \mathbf{0}\\ \mathbf{0} & \mathbf{0} & \boldsymbol{p}_{\xi} & \mathbf{0} & \mathbf{0}\\ \mathbf{0} & \mathbf{0} & \mathbf{0} & \boldsymbol{p}_{\xi} & \mathbf{0}\\ \mathbf{0} & \mathbf{0} & \mathbf{0} & \mathbf{0} & \boldsymbol{p}_{\xi}\end{bmatrix},\ \boldsymbol{A}_{\eta}=\boldsymbol{p}_{\eta}\otimes\boldsymbol{E},\ \boldsymbol{A}_{\xi\xi}=\boldsymbol{A}_{\xi}\cdot\boldsymbol{A}_{\xi}, \boldsymbol{A}_{\eta\eta}=\boldsymbol{A}_{\eta}\cdot\boldsymbol{A}_{\eta}, \boldsymbol{A}_{\xi\eta}=\boldsymbol{A}_{\xi}\cdot\boldsymbol{A}_{\eta} \tag{21}$$

where $\mathbf{0}$ represents a 5×5 zero matrix, $\boldsymbol{E}$ is a 5×5 identity matrix, and the submatrices $\boldsymbol{p}_{\xi}$ and $\boldsymbol{p}_{\eta}$ are expressed as follows:

$$\boldsymbol{p}_{\eta}=\boldsymbol{p}_{\xi}=\begin{bmatrix}-p_1 & p_{11} & -p_4 & p_{10} & -p_2\\ -p_9 & 0 & p_7 & -p_5 & p_8\\ p_3 & -p_6 & 0 & p_6 & -p_3\\ -p_8 & p_5 & -p_7 & 0 & p_9\\ p_2 & -p_{10} & p_4 & -p_{11} & p_1\end{bmatrix} \tag{22}$$

The independent components $p_1\sim p_{11}$ are as follows: $p_1=5$, $p_2=\frac{1}{2}$, $p_3=\frac{3}{8}$, $p_4=\frac{8}{3}$, $p_5=\frac{\sqrt{21}}{6}$, $p_6=\frac{7\sqrt{21}}{24}$, $p_7=\frac{8\sqrt{21}}{21}$, $p_8=\frac{3}{4}-\frac{3\sqrt{21}}{28}$, $p_9=\frac{3}{4}+\frac{3\sqrt{21}}{28}$, $p_{10}=\frac{49}{12}-\frac{7\sqrt{21}}{12}$, $p_{11}=\frac{49}{12}+\frac{7\sqrt{21}}{12}$.

To ensure the continuity of w_s and w_b, a transformation is introduced:

$$\boldsymbol{\Delta}_N = \boldsymbol{B}\boldsymbol{\Delta}_G \tag{23}$$

where $\boldsymbol{B}$ is the transformation matrix provided in Appendix B, and $\boldsymbol{\Delta}_N$ represents the element nodal displacement vector. $\boldsymbol{\Delta}_N$ represents $\boldsymbol{W}_{bN}$ or $\boldsymbol{W}_{sN}$ vector when Δ is w_b or w_s, respectively.

$$\begin{aligned}\boldsymbol{\Delta}_N = \Big[&\langle\Delta\rangle_{11}\ \langle\Delta_{,\xi}\rangle_{11}\ \langle\Delta_{,\eta}\rangle_{11}\ \langle\Delta_{,\xi\eta}\rangle_{11}\ \langle\Delta\rangle_{31}\ \langle\Delta_{,\eta}\rangle_{31}\ \langle\Delta\rangle_{51}\ \langle\Delta_{,\xi}\rangle_{51}\ \mathrm{K}\\ &\langle\Delta_{,\eta}\rangle_{51}\ \langle\Delta_{,\xi\eta}\rangle_{51}\ \langle\Delta\rangle_{53}\ \langle\Delta_{,\xi}\rangle_{53}\ \langle\Delta\rangle_{55}\ \langle\Delta_{,\xi}\rangle_{55}\ \langle\Delta_{,\eta}\rangle_{55}\ \langle\Delta_{,\xi\eta}\rangle_{55}\ \mathrm{K}\\ &\langle\Delta\rangle_{35}\ \langle\Delta_{,\eta}\rangle_{35}\ \langle\Delta\rangle_{15}\ \langle\Delta_{,\xi}\rangle_{15}\ \langle\Delta_{,\eta}\rangle_{15}\ \langle\Delta_{,\xi\eta}\rangle_{15}\ \langle\Delta\rangle_{13}\ \langle\Delta_{,\xi}\rangle_{13}\ \langle\Delta\rangle_{33}\Big]^{\mathrm{T}}\end{aligned} \tag{24}$$

The kinetic energy expression in Eq. (13) can be discretized using the form of Eq. (25) by DQ rule:

$$\begin{aligned}\Pi_k = &\left(\dot{\boldsymbol{W}}_{bN}\right)^T\left(\boldsymbol{B}^{-1}\right)^T\begin{bmatrix}\left(\boldsymbol{A}_\eta\right)^{\mathrm{T}}\boldsymbol{\alpha}_1\boldsymbol{Q}\boldsymbol{J}_d\boldsymbol{A}_\eta+\left(\boldsymbol{A}_\xi\right)^{\mathrm{T}}\boldsymbol{\alpha}_2\boldsymbol{Q}\boldsymbol{J}_d\boldsymbol{A}_\xi+\\ \left(\boldsymbol{A}_\eta\right)^{\mathrm{T}}\boldsymbol{\alpha}_5\boldsymbol{Q}\boldsymbol{J}_d\boldsymbol{A}_\xi+\boldsymbol{\alpha}_7\boldsymbol{Q}\boldsymbol{J}_d+\boldsymbol{\alpha}_8\boldsymbol{Q}\boldsymbol{J}_d\end{bmatrix}\boldsymbol{B}^{-1}\dot{\boldsymbol{W}}_{bN}+\\ &\left(\dot{\boldsymbol{W}}_{sN}\right)^T\left(\boldsymbol{B}^{-1}\right)^T\left[\left(\boldsymbol{A}_\eta\right)^{\mathrm{T}}\boldsymbol{\alpha}_3\boldsymbol{Q}\boldsymbol{J}_d\boldsymbol{A}_\eta+\left(\boldsymbol{A}_\xi\right)^{\mathrm{T}}\boldsymbol{\alpha}_4\boldsymbol{Q}\boldsymbol{J}_d\boldsymbol{A}_\xi+\left(\boldsymbol{A}_\eta\right)^{\mathrm{T}}\boldsymbol{\alpha}_6\boldsymbol{Q}\boldsymbol{J}_d\boldsymbol{A}_\xi\right]\boldsymbol{B}^{-1}\dot{\boldsymbol{W}}_{sN}+\\ &\left(\dot{\boldsymbol{W}}_{sN}\right)^T\left(\boldsymbol{B}^{-1}\right)^{\mathrm{T}}\boldsymbol{\alpha}_9\boldsymbol{Q}\boldsymbol{J}_d\boldsymbol{B}^{-1}\dot{\boldsymbol{W}}_{bN}\end{aligned} \tag{25}$$

The diagonal matrices $\boldsymbol{\alpha}_n$ (n = 1~9) and $\boldsymbol{J}_d$ are both 25×25 diagonal matrices, as follows:

$$\boldsymbol{\alpha}_n = diag\left(\left(\alpha_n\right)_{11},\mathrm{K},\left(\alpha_n\right)_{ij},\mathrm{K}\left(\alpha_n\right)_{55}\right)\ \text{with}\ \ ij=12:\ 51,\ 12:\ 52,\ 13:\ 53,\ 14:\ 54,\ 15:\ 54 \tag{26}$$

$$\boldsymbol{J}_d = diag\left(\left|\boldsymbol{J}\right|_{11},\mathrm{K},\left|\boldsymbol{J}\right|_{ij},\mathrm{K}\left|\boldsymbol{J}\right|_{55}\right)\ \text{with}\ \ ij=12:\ 51,\ 12:\ 52,\ 13:\ 53,\ 14:\ 54,\ 15:\ 54 \tag{27}$$

where $(\alpha_n)_{ij}$ represents the value of coefficient α_n at the ij^{th} quadrature point.

Based on the principle of minimum potential energy, the resulting element mass matrix is formulated as follows:

$$\boldsymbol{M}^e=\begin{bmatrix}\boldsymbol{M}_{11}^e & \boldsymbol{M}_{12}^e\\ \boldsymbol{M}_{21}^e & \boldsymbol{M}_{22}^e\end{bmatrix},\ \text{where}\ \boldsymbol{M}_{11}^e=\frac{\partial^2\Pi_k}{\partial\dot{\boldsymbol{W}}_{bN}\partial\dot{\boldsymbol{W}}_{bN}},\ \boldsymbol{M}_{12}^e=\frac{\partial^2\Pi_k}{\partial\dot{\boldsymbol{W}}_{bN}\partial\dot{\boldsymbol{W}}_{sN}},\ \boldsymbol{M}_{21}^e=\boldsymbol{M}_{12}^e,\ \boldsymbol{M}_{22}^e=\frac{\partial^2\Pi_k}{\partial\dot{\boldsymbol{W}}_{sN}\partial\dot{\boldsymbol{W}}_{sN}} \tag{28}$$

where $\boldsymbol{M}^e$ is a 50×50 square matrix, composed of individual 25×25 submatrices.

Similarly, a strain energy term in Eq. (15) is discretized using Eq. (29), based on the DQ rule such as:

$$\int_{-1}^{1}\int_{-1}^{1}\beta_1 w_{b,\eta\eta}w_{s,\xi\eta}\left|\boldsymbol{J}\right|\mathrm{d}\xi\mathrm{d}\eta=\left(\boldsymbol{W}_{bN}\right)^T\left(\boldsymbol{B}^{-1}\right)^T\left(\boldsymbol{A}_{\eta\eta}\right)^T\boldsymbol{\beta}_1\boldsymbol{Q}\boldsymbol{J}_d\boldsymbol{A}_{\xi\eta}\boldsymbol{B}^{-1}\boldsymbol{W}_{sN} \tag{29}$$

Like $\boldsymbol{\beta}_1$ in Eq. (29), $\boldsymbol{\beta}_n$ (n = 1~55) in Eq. (15) is a 25×25 diagonal matrix, where the diagonal elements represent the values of the β_n coefficients at the 25 quadrature points, and all off-diagonal elements are zero:

$$\boldsymbol{\beta}_n = diag\left(\left(\beta_n\right)_{11},\mathrm{K},\left(\beta_n\right)_{ij},\mathrm{K}\left(\beta_n\right)_{55}\right),\ \text{with}\ \ ij=12:\ 51,\ 12:\ 52,\ 13:\ 53,\ 14:\ 54,\ 15:\ 54 \tag{30}$$

Based on the discretized potential functional and the principle of minimum potential energy, the stiffness matrix is expressed as shown in Eq. (31):

$$\boldsymbol{K}^e=\begin{bmatrix}\boldsymbol{K}_{11}^e & \boldsymbol{K}_{12}^e\\ \boldsymbol{K}_{21}^e & \boldsymbol{K}_{22}^e\end{bmatrix},\ \text{where}\ \boldsymbol{K}_{11}^e=\frac{\partial^2\Pi_s}{\partial\boldsymbol{W}_{bN}\partial\boldsymbol{W}_{bN}},\ \boldsymbol{K}_{12}^e=\frac{\partial^2\Pi_s}{\partial\boldsymbol{W}_{bN}\partial\boldsymbol{W}_{sN}},\ \boldsymbol{K}_{21}^e=\boldsymbol{K}_{12}^e,\ \boldsymbol{K}_{22}^e=\frac{\partial^2\Pi_s}{\partial\boldsymbol{W}_{sN}\partial\boldsymbol{W}_{sN}} \tag{31}$$

where $\boldsymbol{K}^e$ is a 50×50 square matrix, and the individual block matrices are 25×25 square matrices.

3.3 Implementation of matrices assembly and boundary condition

In the local coordinate system, the DOFs at corner nodes include four components: [Δ, $\Delta_{,\xi}$, $\Delta_{,\eta}$, $\Delta_{,\xi\eta}$]. For middle nodes parallel to the ξ-axis, the DOFs are [Δ, $\Delta_{,\eta}$], while those parallel to the η-axis have [Δ, $\Delta_{,\xi}$]. The center node has a single DOF Δ. In the global coordinate system, corner nodes are associated with six DOFs: [Δ, $\Delta_{,x}$, $\Delta_{,y}$, $\Delta_{,xy}$, $\Delta_{,xx}$, $\Delta_{,yy}$]. Here, Δ represents either w_b or w_s. Given this distinction, the order of the element matrix in the local coordinate system differs from that in the global coordinate system. To reconcile this discrepancy, a dimensionality-reduction strategy is adopted to ensure the element matrix in the global coordinate system has 50 DOFs, as depicted in Fig. 3.

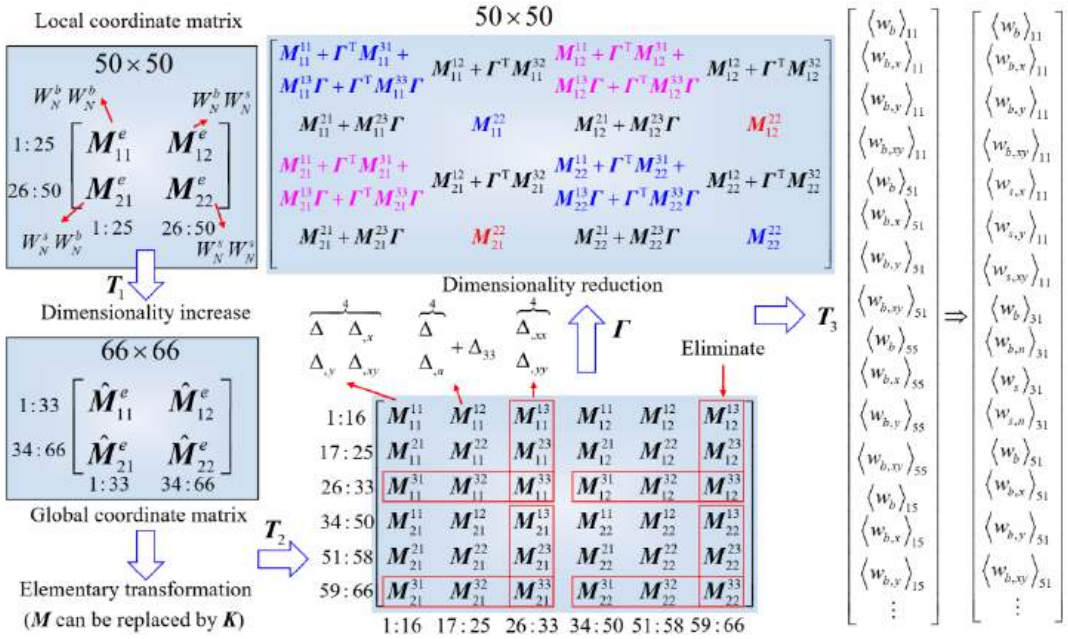

Fig. 3 Transformation scheme for dimensionality increase and reduction between element matrices

When transitioning from local to global coordinates, the number of DOFs at the corner nodes increases. The relationships between derivatives of various orders in the two coordinate systems can be derived using the chain rule, as formulated in Eq. (32) and Eq. (33):

At corner nodes:

$$\begin{aligned}&\Delta=\Delta,\quad \Delta_{,\xi}=\Delta_{,x}x_{,\xi}+\Delta_{,y}y_{,\xi},\quad \Delta_{,\eta}=\Delta_{,x}x_{,\eta}+\Delta_{,y}y_{,\eta}\\&\Delta_{,\xi\eta}=x_{,\eta}x_{,\xi}\Delta_{,xx}+y_{,\eta}y_{,\xi}\Delta_{,yy}+x_{,\eta}y_{,\xi}\Delta_{,xy}+x_{,\xi}y_{,\eta}\Delta_{,xy}+\Delta_{,x}x_{,\xi\eta}+\Delta_{,y}y_{,\xi\eta}\end{aligned}\tag{32}$$

At middle nodes:

$$\Delta=\Delta,\quad\begin{aligned}\Delta_{,\xi}&=\left[|\mathbf{J}|\Delta_{,n}-\Delta_{,\eta}\left(x_{,\xi}n_y-y_{,\xi}n_x\right)\right]\Big/\left(y_{,\eta}n_x-x_{,\eta}n_y\right),\quad(\xi=\pm1)\\\Delta_{,\eta}&=\left[|\mathbf{J}|\Delta_{,n}-\Delta_{,\xi}\left(y_{,\eta}n_x-x_{,\eta}n_y\right)\right]\Big/\left(x_{,\xi}n_y-y_{,\xi}n_x\right),\quad(\eta=\pm1)\end{aligned}\tag{33}$$

As illustrated in Fig. 4, the displacement field along each edge is expressed using Lagrange interpolation functions, ensuring a continuous and smooth approximation of the field variables. Consequently, the tangential derivatives of the transverse displacement at the middle node of the edge can be computed using the derivatives of the Lagrange functions. the normal derivatives along corresponding edges of adjacent elements have opposite directions.

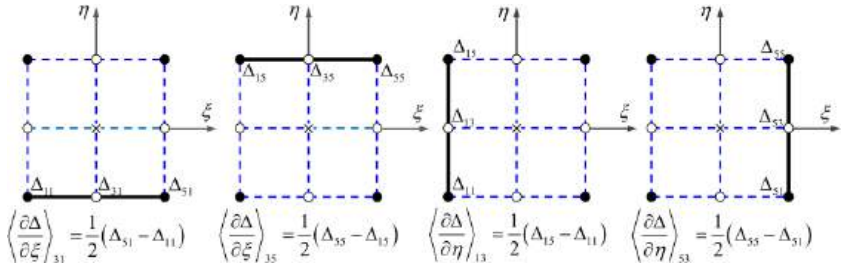

Fig. 4 Lagrange interpolation on the middle node of the element edge

Based on Eq. (32) and Eq. (33), the 25 DOFs associated with the 9 nodes of an element are expressed through 25 equations, as detailed in Appendix C, resulting in the global nodal 33×1 DOF vector, as shown in Eq. (34). By extracting the coefficients of the global DOFs from these 25 equations, a 25×33 transformation matrix, denoted as $\boldsymbol{T}_1$, is constructed.

$$\begin{aligned}
\tilde{\Delta}_N^G &= \Delta_N^{\mathrm{T}} \boldsymbol{T}_1, \text{ where} \\
\tilde{\Delta}_N &= \Big[\langle \Delta \rangle_{11} \ \langle \Delta_{,x} \rangle_{11} \ \langle \Delta_{,y} \rangle_{11} \ \langle \Delta_{,xy} \rangle_{11} \ \langle \Delta_{,xx} \rangle_{11} \ \langle \Delta_{,yy} \rangle_{11} \ \langle \Delta \rangle_{31} \ \langle \Delta_{,n} \rangle_{31} \ \mathrm{K} \\
&\quad \langle \Delta \rangle_{51} \ \langle \Delta_{,x} \rangle_{51} \ \langle \Delta_{,y} \rangle_{51} \ \langle \Delta_{,xy} \rangle_{51} \ \langle \Delta_{,xx} \rangle_{51} \ \langle \Delta_{,yy} \rangle_{51} \ \langle \Delta \rangle_{53} \ \langle \Delta_{,n} \rangle_{53} \ \mathrm{K} \\
&\quad \langle \Delta \rangle_{55} \ \langle \Delta_{,x} \rangle_{55} \ \langle \Delta_{,y} \rangle_{55} \ \langle \Delta_{,xy} \rangle_{55} \ \langle \Delta_{,xx} \rangle_{55} \ \langle \Delta_{,yy} \rangle_{55} \ \langle \Delta \rangle_{35} \ \langle \Delta_{,n} \rangle_{35} \ \mathrm{K} \\
&\quad \langle \Delta \rangle_{15} \ \langle \Delta_{,x} \rangle_{15} \ \langle \Delta_{,y} \rangle_{15} \ \langle \Delta_{,xy} \rangle_{15} \ \langle \Delta_{,xx} \rangle_{15} \ \langle \Delta_{,yy} \rangle_{15} \ \langle \Delta \rangle_{13} \ \langle \Delta_{,n} \rangle_{13} \ \langle \Delta \rangle_{33} \Big]^{\mathrm{T}}
\end{aligned} \tag{34}$$

To achieve dimensionality reduction, the global nodal vector in Eq. (34) must be modified to eliminate the redundant second-order derivatives at the four corner nodes. Initially, the redundant second-order derivatives at the four corner nodes are relocated to the end of the vector. The DOFs at the four corner nodes [Δ, $\Delta_{,x}$, $\Delta_{,y}$, $\Delta_{,xy}$] are arranged first, followed by the DOFs at the four middle nodes [Δ, $\Delta_{,n}$]. Finally, the second-order derivatives corresponding to the corner nodes [$\Delta_{,xx}$, $\Delta_{,yy}$], are placed at the end. This operation involves applying elementary row operations on the Δ_N^G vector using the 33×33 matrix $\boldsymbol{T}_2$, as shown in Eq. (35).

$$\begin{aligned}
\bar{\Delta}_N &= \boldsymbol{T}_2^{\mathrm{T}} \tilde{\Delta}_N \boldsymbol{T}_2 \\
&= [\langle \Delta \rangle_{11} \ \langle \Delta_{,x} \rangle_{11} \ \langle \Delta_{,y} \rangle_{11} \ \langle \Delta_{,xy} \rangle_{11} \ \langle \Delta \rangle_{51} \ \langle \Delta_{,x} \rangle_{51} \ \langle \Delta_{,y} \rangle_{51} \ \langle \Delta_{,xy} \rangle_{51} \ \langle \Delta \rangle_{55} \ \langle \Delta_{,x} \rangle_{55} \ \langle \Delta_{,y} \rangle_{55} \ \langle \Delta_{,xy} \rangle_{55} \ \mathrm{K} \\
&\quad \langle \Delta \rangle_{15} \ \langle \Delta_{,x} \rangle_{15} \ \langle \Delta_{,y} \rangle_{15} \ \langle \Delta_{,xy} \rangle_{15} \ \langle \Delta \rangle_{31} \ \langle \Delta_{,n} \rangle_{31} \ \langle \Delta \rangle_{53} \ \langle \Delta_{,n} \rangle_{53} \ \langle \Delta \rangle_{35} \ \langle \Delta_{,n} \rangle_{35} \ \langle \Delta \rangle_{13} \ \langle \Delta_{,n} \rangle_{13} \ \langle \Delta \rangle_{33} \ \mathrm{K} \\
&\quad \langle \Delta_{,xx} \rangle_{11} \ \langle \Delta_{,yy} \rangle_{11} \ \langle \Delta_{,xx} \rangle_{51} \ \langle \Delta_{,yy} \rangle_{51} \ \langle \Delta_{,xx} \rangle_{55} \ \langle \Delta_{,yy} \rangle_{55} \ \langle \Delta_{,xx} \rangle_{15} \ \langle \Delta_{,yy} \rangle_{15}]^{\mathrm{T}}
\end{aligned} \tag{35}$$

In Eq. (35), $\bar{\Delta}_N$ comprises three components as follows:

$$\begin{aligned}
\bar{\Delta}_{N(1)} &= \Big[\langle \Delta \rangle_{11} \ \langle \Delta_{,x} \rangle_{11} \ \langle \Delta_{,y} \rangle_{11} \ \langle \Delta_{,xy} \rangle_{11} \ \langle \Delta \rangle_{51} \ \langle \Delta_{,x} \rangle_{51} \ \langle \Delta_{,y} \rangle_{51} \ \langle \Delta_{,xy} \rangle_{51} \ \mathrm{K} \\
&\qquad \langle \Delta \rangle_{55} \ \langle \Delta_{,x} \rangle_{55} \ \langle \Delta_{,y} \rangle_{55} \ \langle \Delta_{,xy} \rangle_{55} \ \langle \Delta \rangle_{15} \ \langle \Delta_{,x} \rangle_{15} \ \langle \Delta_{,y} \rangle_{15} \ \langle \Delta_{,xy} \rangle_{15} \Big]^{\mathrm{T}}, \\
\bar{\Delta}_{N(2)} &= \Big[\langle \Delta \rangle_{31} \ \langle \Delta_{,n} \rangle_{31} \ \langle \Delta \rangle_{53} \ \langle \Delta_{,n} \rangle_{53} \ \langle \Delta \rangle_{35} \ \langle \Delta_{,n} \rangle_{35} \ \langle \Delta \rangle_{13} \ \langle \Delta_{,n} \rangle_{13} \ \langle \Delta \rangle_{33} \Big]^{\mathrm{T}}, \\
\bar{\Delta}_{N(3)} &= \Big[\langle \Delta_{,xx} \rangle_{11} \ \langle \Delta_{,yy} \rangle_{11} \ \langle \Delta_{,xx} \rangle_{51} \ \langle \Delta_{,yy} \rangle_{51} \ \langle \Delta_{,xx} \rangle_{55} \ \langle \Delta_{,yy} \rangle_{55} \ \langle \Delta_{,xx} \rangle_{15} \ \langle \Delta_{,yy} \rangle_{15} \Big]^{\mathrm{T}}
\end{aligned} \tag{36}$$

where the vector $\bar{\Delta}_{N(3)}$ can be expressed as a product of the vector $\bar{\Delta}_{N(1)}$, as follows:

$$\bar{\Delta}_{N(3)} = \boldsymbol{\Gamma} \cdot \bar{\Delta}_{N(1)}, \text{ where } \boldsymbol{\Gamma} = \boldsymbol{\Gamma}_1 \cdot \boldsymbol{\Gamma}_2^{-1} \tag{37}$$

As depicted in Eq. (37), the 8×16 matrix $\boldsymbol{\Gamma}$ is a transformation matrix based on a 16-term polynomial that satisfies the compatibility condition. Eqs. (38a) and (38b) provide the explicit forms for $\boldsymbol{\Gamma}_1$ and $\boldsymbol{\Gamma}_2$, respectively.

$$\boldsymbol{\Gamma}_1 = \begin{bmatrix}
0 & 0 & 0 & 2 & 0 & 0 & 6x_1 & 2y_1 & 0 & 0 & 6x_1y_1 & 2y_1^2 & 0 & 6x_1y_1^2 & 2y_1^3 & 6x_1y_1^3 \\
0 & 0 & 0 & 0 & 0 & 2 & 0 & 0 & 2x_1 & 6y_1 & 0 & 2x_1^2 & 6x_1y_1 & 2x_1^3 & 6x_1^2y_1 & 6x_1^3y_1 \\
0 & 0 & 0 & 2 & 0 & 0 & 6x_3 & 2y_3 & 0 & 0 & 6x_3y_3 & 2y_3^2 & 0 & 6x_3y_3^2 & 2y_3^3 & 6x_3y_3^3 \\
0 & 0 & 0 & 0 & 0 & 2 & 0 & 0 & 2x_3 & 6y_3 & 0 & 2x_3^2 & 6x_3y_3 & 2x_3^3 & 6x_3^2y_3 & 6x_3^3y_3 \\
0 & 0 & 0 & 2 & 0 & 0 & 6x_5 & 2y_5 & 0 & 0 & 6x_5y_5 & 2y_5^2 & 0 & 6x_5y_5^2 & 2y_5^3 & 6x_5y_5^3 \\
0 & 0 & 0 & 0 & 0 & 2 & 0 & 0 & 2x_5 & 6y_5 & 0 & 2x_5^2 & 6x_5y_5 & 2x_5^3 & 6x_5^2y_5 & 6x_5^3y_5 \\
0 & 0 & 0 & 2 & 0 & 0 & 6x_7 & 2y_7 & 0 & 0 & 6x_7y_7 & 2y_7^2 & 0 & 6x_7y_7^2 & 2y_7^3 & 6x_7y_7^3 \\
0 & 0 & 0 & 0 & 0 & 2 & 0 & 0 & 2x_7 & 6y_7 & 0 & 2x_7^2 & 6x_7y_7 & 2x_7^3 & 6x_7^2y_7 & 6x_7^3y_7
\end{bmatrix} \tag{38a}$$

$$\boldsymbol{\Gamma}_2 = \begin{bmatrix}
1 & x_1 & y_1 & x_1^2 & x_1y_1 & y_1^2 & x_1^3 & x_1^2y_1 & x_1y_1^2 & y_1^3 & x_1^3y_1 & x_1^2y_1^2 & x_1y_1^3 & x_1^3y_1^2 & x_1^2y_1^3 & x_1^3y_1^3 \\
0 & 1 & 0 & 2x_1 & y_1 & 0 & 3x_1^2 & 2x_1y_1 & y_1^2 & 0 & 3x_1^2y_1 & 2x_1y_1^2 & y_1^3 & 3x_1^2y_1^2 & 2x_1y_1^3 & 3x_1^2y_1^3 \\
0 & 0 & 1 & 0 & x_1 & 2y_1 & 0 & x_1^2 & 2x_1y_1 & 3y_1^2 & x_1^3 & 2x_1^2y_1 & 3x_1y_1^2 & 2x_1^3y_1 & 3x_1^2y_1^2 & 3x_1^3y_1^2 \\
0 & 0 & 0 & 0 & 1 & 0 & 0 & 2x_1 & 2y_1 & 0 & 3x_1^2 & 4x_1y_1 & 3y_1^2 & 6x_1^2y_1 & 6x_1y_1^2 & 9x_1^2y_1^2 \\
1 & x_3 & y_3 & x_3^2 & x_3y_3 & y_3^2 & x_3^3 & x_3^2y_3 & x_3y_3^2 & y_3^3 & x_3^3y_3 & x_3^2y_3^2 & x_3y_3^3 & x_3^3y_3^2 & x_3^2y_3^3 & x_3^3y_3^3 \\
0 & 1 & 0 & 2x_3 & y_3 & 0 & 3x_3^2 & 2x_3y_3 & y_3^2 & 0 & 3x_3^2y_3 & 2x_3y_3^2 & y_3^3 & 3x_3^2y_3^2 & 2x_3y_3^3 & 3x_3^2y_3^3 \\
0 & 0 & 1 & 0 & x_3 & 2y_3 & 0 & x_3^2 & 2x_3y_3 & 3y_3^2 & x_3^3 & 2x_3^2y_3 & 3x_3y_3^2 & 2x_3^3y_3 & 3x_3^2y_3^2 & 3x_3^3y_3^2 \\
0 & 0 & 0 & 0 & 1 & 0 & 0 & 2x_3 & 2y_3 & 0 & 3x_3^2 & 4x_3y_3 & 3y_3^2 & 6x_3^2y_3 & 6x_3y_3^2 & 9x_3^2y_3^2 \\
1 & x_5 & y_5 & x_5^2 & x_5y_5 & y_5^2 & x_5^3 & x_5^2y_5 & x_5y_5^2 & y_5^3 & x_5^3y_5 & x_5^2y_5^2 & x_5y_5^3 & x_5^3y_5^2 & x_5^2y_5^3 & x_5^3y_5^3 \\
0 & 1 & 0 & 2x_5 & y_5 & 0 & 3x_5^2 & 2x_5y_5 & y_5^2 & 0 & 3x_5^2y_5 & 2x_5y_5^2 & y_5^3 & 3x_5^2y_5^2 & 2x_5y_5^3 & 3x_5^2y_5^3 \\
0 & 0 & 1 & 0 & x_5 & 2y_5 & 0 & x_5^2 & 2x_5y_5 & 3y_5^2 & x_5^3 & 2x_5^2y_5 & 3x_5y_5^2 & 2x_5^3y_5 & 3x_5^2y_5^2 & 3x_5^3y_5^2 \\
0 & 0 & 0 & 0 & 1 & 0 & 0 & 2x_5 & 2y_5 & 0 & 3x_5^2 & 4x_5y_5 & 3y_5^2 & 6x_5^2y_5 & 6x_5y_5^2 & 9x_5^2y_5^2 \\
1 & x_7 & y_7 & x_7^2 & x_7y_7 & y_7^2 & x_7^3 & x_7^2y_7 & x_7y_7^2 & y_7^3 & x_7^3y_7 & x_7^2y_7^2 & x_7y_7^3 & x_7^3y_7^2 & x_7^2y_7^3 & x_7^3y_7^3 \\
0 & 1 & 0 & 2x_7 & y_7 & 0 & 3x_7^2 & 2x_7y_7 & y_7^2 & 0 & 3x_7^2y_7 & 2x_7y_7^2 & y_7^3 & 3x_7^2y_7^2 & 2x_7y_7^3 & 3x_7^2y_7^3 \\
0 & 0 & 1 & 0 & x_7 & 2y_7 & 0 & x_7^2 & 2x_7y_7 & 3y_7^2 & x_7^3 & 2x_7^2y_7 & 3x_7y_7^2 & 2x_7^3y_7 & 3x_7^2y_7^2 & 3x_7^3y_7^2 \\
0 & 0 & 0 & 0 & 1 & 0 & 0 & 2x_7 & 2y_7 & 0 & 3x_7^2 & 4x_7y_7 & 3y_7^2 & 6x_7^2y_7 & 6x_7y_7^2 & 9x_7^2y_7^2
\end{bmatrix} \tag{38b}$$

where the four nodal coordinates (x_1, y_1), (x_3, y_3), (x_5, y_5), and (x_7, y_7) within the element are used.

After obtaining the dimensionality-increase transformation matrix $\boldsymbol{T}_1$ and the elementary transformation matrix $\boldsymbol{T}_2$, the element mass matrix $\hat{\boldsymbol{M}}_G^e$ and the element stiffness matrix $\hat{\boldsymbol{K}}_G^e$ in the global coordinate system are expressed as:

$$\hat{\boldsymbol{M}}_G^e = \begin{bmatrix} \boldsymbol{T}_2^{\mathrm{T}}\boldsymbol{T}_1^{\mathrm{T}}\boldsymbol{M}_{11}^e\boldsymbol{T}_1\boldsymbol{T}_2 & \boldsymbol{T}_2^{\mathrm{T}}\boldsymbol{T}_1^{\mathrm{T}}\boldsymbol{M}_{12}^e\boldsymbol{T}_1\boldsymbol{T}_2 \\ \boldsymbol{T}_2^{\mathrm{T}}\boldsymbol{T}_1^{\mathrm{T}}\boldsymbol{M}_{21}^e\boldsymbol{T}_1\boldsymbol{T}_2 & \boldsymbol{T}_2^{\mathrm{T}}\boldsymbol{T}_1^{\mathrm{T}}\boldsymbol{M}_{22}^e\boldsymbol{T}_1\boldsymbol{T}_2 \end{bmatrix} \qquad \hat{\boldsymbol{K}}_G^e = \begin{bmatrix} \boldsymbol{T}_2^{\mathrm{T}}\boldsymbol{T}_1^{\mathrm{T}}\boldsymbol{K}_{11}^e\boldsymbol{T}_1\boldsymbol{T}_2 & \boldsymbol{T}_2^{\mathrm{T}}\boldsymbol{T}_1^{\mathrm{T}}\boldsymbol{K}_{12}^e\boldsymbol{T}_1\boldsymbol{T}_2 \\ \boldsymbol{T}_2^{\mathrm{T}}\boldsymbol{T}_1^{\mathrm{T}}\boldsymbol{K}_{21}^e\boldsymbol{T}_1\boldsymbol{T}_2 & \boldsymbol{T}_2^{\mathrm{T}}\boldsymbol{T}_1^{\mathrm{T}}\boldsymbol{K}_{22}^e\boldsymbol{T}_1\boldsymbol{T}_2 \end{bmatrix}$$

$$= \begin{bmatrix}
\boldsymbol{M}_{11}^{11} & \boldsymbol{M}_{11}^{12} & \boldsymbol{M}_{11}^{13} & \boldsymbol{M}_{12}^{11} & \boldsymbol{M}_{12}^{12} & \boldsymbol{M}_{12}^{13} \\
\boldsymbol{M}_{11}^{21} & \boldsymbol{M}_{11}^{22} & \boldsymbol{M}_{11}^{23} & \boldsymbol{M}_{12}^{21} & \boldsymbol{M}_{12}^{22} & \boldsymbol{M}_{12}^{23} \\
\boldsymbol{M}_{11}^{31} & \boldsymbol{M}_{11}^{32} & \boldsymbol{M}_{11}^{33} & \boldsymbol{M}_{12}^{31} & \boldsymbol{M}_{12}^{32} & \boldsymbol{M}_{12}^{33} \\
\boldsymbol{M}_{21}^{11} & \boldsymbol{M}_{21}^{12} & \boldsymbol{M}_{21}^{13} & \boldsymbol{M}_{22}^{11} & \boldsymbol{M}_{22}^{12} & \boldsymbol{M}_{22}^{13} \\
\boldsymbol{M}_{21}^{21} & \boldsymbol{M}_{21}^{22} & \boldsymbol{M}_{21}^{23} & \boldsymbol{M}_{22}^{21} & \boldsymbol{M}_{22}^{22} & \boldsymbol{M}_{22}^{23} \\
\boldsymbol{M}_{21}^{31} & \boldsymbol{M}_{21}^{32} & \boldsymbol{M}_{21}^{33} & \boldsymbol{M}_{22}^{31} & \boldsymbol{M}_{22}^{32} & \boldsymbol{M}_{22}^{33}
\end{bmatrix}, = \begin{bmatrix}
\boldsymbol{K}_{11}^{11} & \boldsymbol{K}_{11}^{12} & \boldsymbol{K}_{11}^{13} & \boldsymbol{K}_{12}^{11} & \boldsymbol{K}_{12}^{12} & \boldsymbol{K}_{12}^{13} \\
\boldsymbol{K}_{11}^{21} & \boldsymbol{K}_{11}^{22} & \boldsymbol{K}_{11}^{23} & \boldsymbol{K}_{12}^{21} & \boldsymbol{K}_{12}^{22} & \boldsymbol{K}_{12}^{23} \\
\boldsymbol{K}_{11}^{31} & \boldsymbol{K}_{11}^{32} & \boldsymbol{K}_{11}^{33} & \boldsymbol{K}_{12}^{31} & \boldsymbol{K}_{12}^{32} & \boldsymbol{K}_{12}^{33} \\
\boldsymbol{K}_{21}^{11} & \boldsymbol{K}_{21}^{12} & \boldsymbol{K}_{21}^{13} & \boldsymbol{K}_{22}^{11} & \boldsymbol{K}_{22}^{12} & \boldsymbol{K}_{22}^{13} \\
\boldsymbol{K}_{21}^{21} & \boldsymbol{K}_{21}^{22} & \boldsymbol{K}_{21}^{23} & \boldsymbol{K}_{22}^{21} & \boldsymbol{K}_{22}^{22} & \boldsymbol{K}_{22}^{23} \\
\boldsymbol{K}_{21}^{31} & \boldsymbol{K}_{21}^{32} & \boldsymbol{K}_{21}^{33} & \boldsymbol{K}_{22}^{31} & \boldsymbol{K}_{22}^{32} & \boldsymbol{K}_{22}^{33}
\end{bmatrix} \tag{39}$$

Based on the dimensionality increase outlined in Eq. (39), the matrices for dimensionality reduction in the global coordinate system can be reconstructed using the $\boldsymbol{\Gamma}$ matrix. The final step involves reordering the DOFs according to the node sequence. First, the DOF vector for each element was sorted by the bending components (w_b) for the first 25 DOFs, followed by the shear components (w_s) for the subsequent 25 DOFs. The transformation is carried out by multiplying the element DOF vector by an elementary row transformation 50×50 matrix $\boldsymbol{T}_3$. The final element mass matrix $\boldsymbol{M}_G^e$ and element stiffness matrix $\boldsymbol{K}_G^e$ are then expressed as:

$$\boldsymbol{M}_G^e = \boldsymbol{T}_3^{\mathrm{T}} \begin{bmatrix}
\begin{bmatrix} \boldsymbol{M}_{11}^{11} + \boldsymbol{\Gamma}^{\mathrm{T}}\boldsymbol{M}_{11}^{31} + \\ \boldsymbol{M}_{11}^{13}\boldsymbol{\Gamma} + \boldsymbol{\Gamma}^{\mathrm{T}}\boldsymbol{M}_{11}^{33}\boldsymbol{\Gamma} \end{bmatrix} & \begin{bmatrix} \boldsymbol{M}_{11}^{12} + \boldsymbol{\Gamma}^{\mathrm{T}}\boldsymbol{M}_{11}^{32} \end{bmatrix} & \begin{bmatrix} \boldsymbol{M}_{12}^{11} + \boldsymbol{\Gamma}^{\mathrm{T}}\boldsymbol{M}_{12}^{31} + \\ \boldsymbol{M}_{12}^{13}\boldsymbol{\Gamma} + \boldsymbol{\Gamma}^{\mathrm{T}}\boldsymbol{M}_{12}^{33}\boldsymbol{\Gamma} \end{bmatrix} & \begin{bmatrix} \boldsymbol{M}_{12}^{12} + \boldsymbol{\Gamma}^{\mathrm{T}}\boldsymbol{M}_{12}^{32} \end{bmatrix} \\
\begin{bmatrix} \boldsymbol{M}_{11}^{21} + \boldsymbol{M}_{11}^{23}\boldsymbol{\Gamma} \end{bmatrix} & \begin{bmatrix} \boldsymbol{M}_{11}^{22} \end{bmatrix} & \begin{bmatrix} \boldsymbol{M}_{12}^{21} + \boldsymbol{M}_{12}^{23}\boldsymbol{\Gamma} \end{bmatrix} & \begin{bmatrix} \boldsymbol{M}_{12}^{22} \end{bmatrix} \\
\begin{bmatrix} \boldsymbol{M}_{21}^{11} + \boldsymbol{\Gamma}^{\mathrm{T}}\boldsymbol{M}_{21}^{31} + \\ \boldsymbol{M}_{21}^{13}\boldsymbol{\Gamma} + \boldsymbol{\Gamma}^{\mathrm{T}}\boldsymbol{M}_{21}^{33}\boldsymbol{\Gamma} \end{bmatrix} & \begin{bmatrix} \boldsymbol{M}_{21}^{12} + \boldsymbol{\Gamma}^{\mathrm{T}}\boldsymbol{M}_{21}^{32} \end{bmatrix} & \begin{bmatrix} \boldsymbol{M}_{22}^{11} + \boldsymbol{\Gamma}^{\mathrm{T}}\boldsymbol{M}_{22}^{31} + \\ \boldsymbol{M}_{22}^{13}\boldsymbol{\Gamma} + \boldsymbol{\Gamma}^{\mathrm{T}}\boldsymbol{M}_{22}^{33}\boldsymbol{\Gamma} \end{bmatrix} & \begin{bmatrix} \boldsymbol{M}_{22}^{12} + \boldsymbol{\Gamma}^{\mathrm{T}}\boldsymbol{M}_{22}^{32} \end{bmatrix} \\
\begin{bmatrix} \boldsymbol{M}_{21}^{21} + \boldsymbol{M}_{21}^{23}\boldsymbol{\Gamma} \end{bmatrix} & \begin{bmatrix} \boldsymbol{M}_{21}^{22} \end{bmatrix} & \begin{bmatrix} \boldsymbol{M}_{22}^{21} + \boldsymbol{M}_{22}^{23}\boldsymbol{\Gamma} \end{bmatrix} & \begin{bmatrix} \boldsymbol{M}_{22}^{22} \end{bmatrix}
\end{bmatrix} \boldsymbol{T}_3 \tag{40a}$$

$$\boldsymbol{K}_G^e=\boldsymbol{T}_3^{\mathrm{T}}\begin{bmatrix}\begin{bmatrix}\boldsymbol{K}_{11}^{11}+\boldsymbol{\Gamma}^{\mathrm{T}}\boldsymbol{K}_{11}^{31}+\\ \boldsymbol{K}_{11}^{13}\boldsymbol{\Gamma}+\boldsymbol{\Gamma}^{\mathrm{T}}\boldsymbol{K}_{11}^{33}\boldsymbol{\Gamma}\end{bmatrix} & \left[\boldsymbol{K}_{11}^{12}+\boldsymbol{\Gamma}^{\mathrm{T}}\boldsymbol{K}_{11}^{32}\right] & \begin{bmatrix}\boldsymbol{K}_{12}^{11}+\boldsymbol{\Gamma}^{\mathrm{T}}\boldsymbol{K}_{12}^{31}+\\ \boldsymbol{K}_{12}^{13}\boldsymbol{\Gamma}+\boldsymbol{\Gamma}^{\mathrm{T}}\boldsymbol{K}_{12}^{33}\boldsymbol{\Gamma}\end{bmatrix} & \left[\boldsymbol{K}_{12}^{12}+\boldsymbol{\Gamma}^{\mathrm{T}}\boldsymbol{K}_{12}^{32}\right] \\ \left[\boldsymbol{K}_{11}^{21}+\boldsymbol{K}_{11}^{23}\boldsymbol{\Gamma}\right] & \left[\boldsymbol{K}_{11}^{22}\right] & \left[\boldsymbol{K}_{12}^{21}+\boldsymbol{K}_{12}^{23}\boldsymbol{\Gamma}\right] & \left[\boldsymbol{K}_{12}^{22}\right] \\ \begin{bmatrix}\boldsymbol{K}_{21}^{11}+\boldsymbol{\Gamma}^{\mathrm{T}}\boldsymbol{K}_{21}^{31}+\\ \boldsymbol{K}_{21}^{13}\boldsymbol{\Gamma}+\boldsymbol{\Gamma}^{\mathrm{T}}\boldsymbol{K}_{21}^{33}\boldsymbol{\Gamma}\end{bmatrix} & \left[\boldsymbol{K}_{21}^{12}+\boldsymbol{\Gamma}^{\mathrm{T}}\boldsymbol{K}_{21}^{32}\right] & \begin{bmatrix}\boldsymbol{K}_{22}^{11}+\boldsymbol{\Gamma}^{\mathrm{T}}\boldsymbol{K}_{22}^{31}+\\ \boldsymbol{K}_{22}^{13}\boldsymbol{\Gamma}+\boldsymbol{\Gamma}^{\mathrm{T}}\boldsymbol{K}_{22}^{33}\boldsymbol{\Gamma}\end{bmatrix} & \left[\boldsymbol{K}_{22}^{12}+\boldsymbol{\Gamma}^{\mathrm{T}}\boldsymbol{K}_{22}^{32}\right] \\ \left[\boldsymbol{K}_{21}^{21}+\boldsymbol{K}_{21}^{23}\boldsymbol{\Gamma}\right] & \left[\boldsymbol{K}_{21}^{22}\right] & \left[\boldsymbol{K}_{22}^{21}+\boldsymbol{K}_{22}^{23}\boldsymbol{\Gamma}\right] & \left[\boldsymbol{K}_{22}^{22}\right]\end{bmatrix}\boldsymbol{T}_3 \tag{40b}$$

The global nodal DOF vector $\boldsymbol{\Delta}_N^{Global}$ corresponding to the global mass and stiffness matrices $\boldsymbol{M}_G^e$ and $\boldsymbol{K}_G^e$ is expressed as follows:

$$\begin{aligned}\boldsymbol{\Delta}_N^{Global}=\Big[&\langle\Delta\rangle_{11}\ \langle\Delta_{,x}\rangle_{11}\ \langle\Delta_{,y}\rangle_{11}\ \langle\Delta_{,xy}\rangle_{11}\ \langle\Delta\rangle_{31}\ \langle\Delta_{,n}\rangle_{31}\ \langle\Delta\rangle_{51}\ \langle\Delta_{,x}\rangle_{51}\ \langle\Delta_{,y}\rangle_{51}\ \langle\Delta_{,xy}\rangle_{51}\ \langle\Delta\rangle_{53}\ \langle\Delta_{,n}\rangle_{53}\ \mathrm{K}\\ &\langle\Delta\rangle_{55}\ \langle\Delta_{,x}\rangle_{55}\ \langle\Delta_{,y}\rangle_{55}\ \langle\Delta_{,xy}\rangle_{55}\ \langle\Delta\rangle_{35}\ \langle\Delta_{,n}\rangle_{35}\ \langle\Delta\rangle_{15}\ \langle\Delta_{,x}\rangle_{15}\ \langle\Delta_{,y}\rangle_{15}\ \langle\Delta_{,xy}\rangle_{15}\ \langle\Delta\rangle_{13}\ \langle\Delta_{,n}\rangle_{13}\ \langle\Delta\rangle_{33}\Big]^{\mathrm{T}}\end{aligned} \tag{41}$$

After assembling the global mass matrix $\boldsymbol{M}$ and stiffness matrix $\boldsymbol{K}$, boundary conditions must be applied to the plate. For quadrilateral plates, the normal ($\boldsymbol{n}$) and tangent ($\boldsymbol{\tau}$) vectors of the boundary nodes are not necessarily aligned with the coordinate axes x or y. The clamped and simply supported boundary conditions are defined by Eq. (42).

$$\begin{aligned}C:&\left[w_b,w_s,\frac{\partial w_b}{\partial n},\frac{\partial w_s}{\partial n},\frac{\partial w_b}{\partial \tau},\frac{\partial w_s}{\partial \tau}\right]\ \text{(corner node)}\ \left[w_b,w_s,\frac{\partial w_b}{\partial n},\frac{\partial w_s}{\partial n}\right]\ \text{(middle node)}\\ S:&\left[w_b,w_s,\frac{\partial w_b}{\partial \tau},\frac{\partial w_s}{\partial \tau}\right]\qquad\text{(corner node)}\ \left[w_b,w_s\right]\qquad\text{(middle node)}\end{aligned} \tag{42}$$

where the clamped corner nodal DOF can be arranged as $[w_b,\ w_s,\ \partial w_b/\partial x,\ \partial w_s/\partial x,\ \partial w_b/\partial y,\ \partial w_s/\partial y]$.

Specifically, the derivatives along the tangent ($\boldsymbol{\tau}$) direction can be expressed as a linear combination of the partial derivatives with respect to x and y, as shown in Eq. (43).

$$\begin{aligned}&w_b=0,\frac{\partial w_b}{\partial \tau}=\frac{\partial w_b}{\partial x}\tau_x+\frac{\partial w_b}{\partial y}\tau_y=0,\ \ w_s=0,\frac{\partial w_s}{\partial \tau}=\frac{\partial w_s}{\partial x}\tau_x+\frac{\partial w_s}{\partial y}\tau_y=0\Rightarrow\\ &\begin{bmatrix}1&0&0&0&0&0&0&0\\0&\tau_x&\tau_y&0&0&0&0&0\\0&0&0&0&1&0&0&0\\0&0&0&0&0&\tau_x&\tau_y&0\end{bmatrix}\begin{bmatrix}w_b\\w_{b,x}\\w_{b,y}\\w_{b,xy}\\w_s\\w_{s,x}\\w_{s,y}\\w_{s,xy}\end{bmatrix}=\begin{bmatrix}w_b\\w_{b,x}\tau_x+w_{b,y}\tau_y\\w_s\\w_{s,x}\tau_x+w_{s,y}\tau_y\end{bmatrix}=\begin{bmatrix}0\\0\\0\\0\end{bmatrix}\end{aligned} \tag{43}$$

For a given segment of the boundary, the number of constraints is m, and the total number of nodal DOFs is n. The boundary conditions for the microplate can now be expressed as follows:

$$\boldsymbol{C}_{(\partial A)}\boldsymbol{\Delta}_{all},\ \text{where}\ \boldsymbol{C}_{(\partial A)}=\boldsymbol{U}_{(\partial A)}\boldsymbol{\Sigma}_{(\partial A)}\boldsymbol{V}_{(\partial A)}^{\mathrm{T}},\ \boldsymbol{\Sigma}_{(\partial A)}=\begin{bmatrix}\boldsymbol{\Sigma}_{r\times r}&\boldsymbol{0}_{r\times(n-r)}\\\boldsymbol{0}_{(m-r)\times r}&\boldsymbol{0}_{(m-r)\times(n-r)}\end{bmatrix},\ \boldsymbol{V}_{(\partial A)}^{\mathrm{T}}=\begin{bmatrix}\boldsymbol{V}_{n\times r}&\boldsymbol{V}_{n\times(n-r)}\end{bmatrix}^{\mathrm{T}} \tag{44}$$

where singular value decomposition is performed on the $\mathbf{C}_{(\partial A)}$ matrix.

In Eq. (44), $\boldsymbol{\Delta}_{all}$ is the $n\times1$ nodal DOF vector for all nodes, and $\boldsymbol{C}_{(\partial A)}$ is the $m\times n$ constraint matrix, with m representing the number of constrained nodal DOFs. $\boldsymbol{U}_{(\partial A)}$ is an $m\times m$ unitary matrix, $\boldsymbol{V}_{(\partial A)}$ is another $n\times n$ unitary matrix, and $\boldsymbol{\Sigma}_{(\partial A)}$ is an $m\times n$ rectangular diagonal matrix. As referenced in previous work [47], the dimensionality-reduced global stiffness and mass matrices are given by Eq. (45). This results in an eigenvalue problem for the system vibration equations:

$$\hat{\boldsymbol{K}}=\boldsymbol{V}_{n\times(n-r)}^{T}\boldsymbol{K}\boldsymbol{V}_{n\times(n-r)},\ \hat{\boldsymbol{M}}=\boldsymbol{V}_{n\times(n-r)}^{T}\boldsymbol{M}\boldsymbol{V}_{n\times(n-r)},\ \hat{\boldsymbol{K}}\boldsymbol{X}=\omega^2\hat{\boldsymbol{M}}\boldsymbol{X},\ \left|\hat{\boldsymbol{K}}-\omega^2\hat{\boldsymbol{M}}\right|=0 \tag{45}$$

where the eigenvalues (ω) correspond to the frequencies, and the eigenvectors ($\boldsymbol{X}$) correspond to the matrix of generalized nodal displacements, with each column representing a distinct mode.

4 Application and discussion

4.1 Convergence and verification

In this case, as depicted in Fig. 5a, a thick square microplate (a/b = 1, h/a = 0.2, l/h = 0.5 or 1) is used to validate the convergencies of the present method under SSSS and FSCS boundary conditions. The material properties are as follows: E = 1.44 GPa, v = 0.3, and ρ = 2800 kg/m^3. Convergence characteristics of the first five natural frequencies obtained via the proposed methodology are systematically evaluated. Fig. 6 demonstrates relative error distributions for square microplate frequencies under SSSS and FSCS boundary constraints. Progressive mesh refinement drives frequency convergence toward stabilized values. Notably, accelerated convergence rates are observed for the first five eigenfrequencies across both boundary configurations. Nevertheless, the computationally intensive FSCS case exhibits marginally reduced convergence efficacy relative to the SSSS scenario.

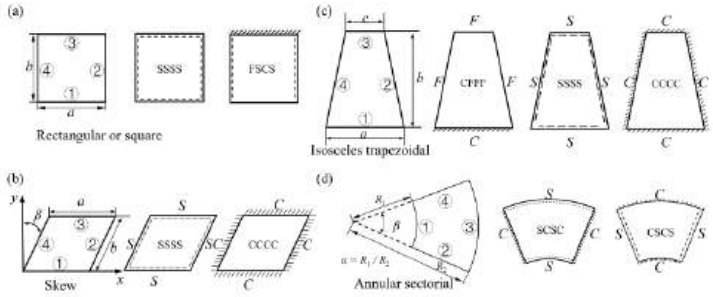

Fig. 5 Plate configuration: (a) Rectangular or square, (b) Skew, (c) Isosceles trapezoidal, and (d) Annular sectorial plates

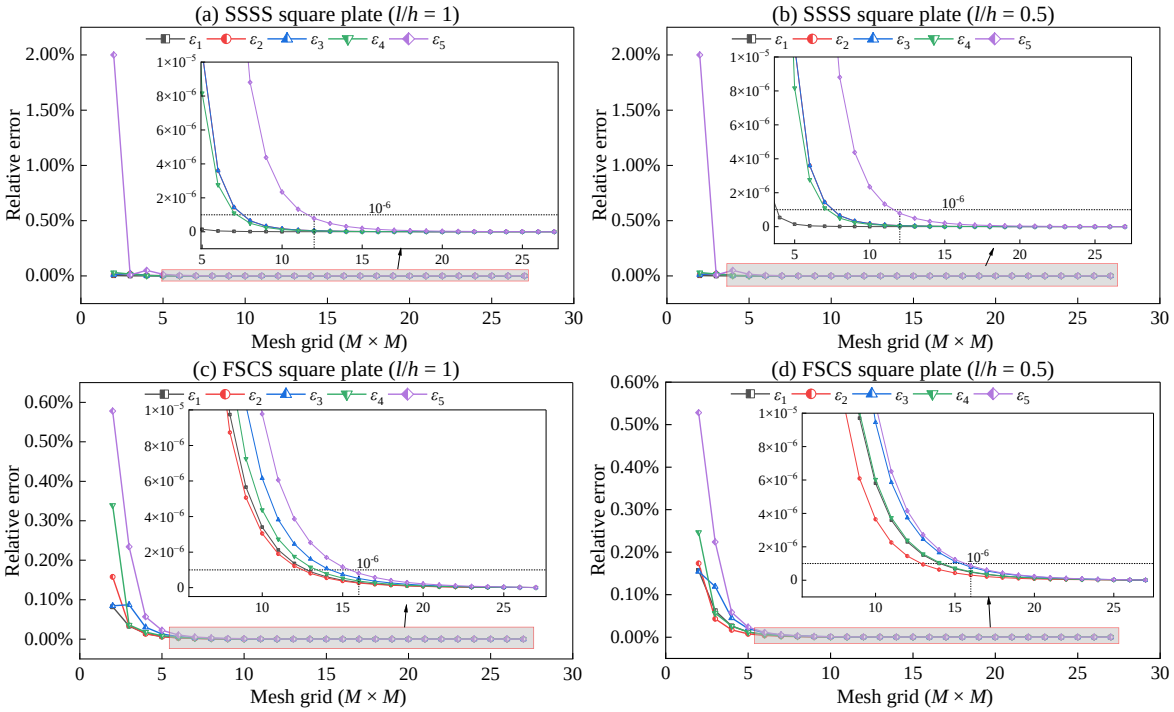

Fig. 6 Convergence of the first five dimensionless frequencies for SSSS and FSCS square plates

A comparison was made with the four-node DQFE from the previous configuration [73] to evaluate the convergence rate of the present method. The DOFs of the $M \times M$ nine-node DQFE and the $N \times N$ four-node DQFE are $2(3M + 2)^2$ and $8(N + 1)^2$, respectively. Under equivalent DOF conditions, Table 1,enumerates corresponding mesh configurations, with log-relative errors calculated using reference solutions, and the common logarithm of the relative error in the dimensionless frequency is calculated using $\delta = \lg[|\varpi - \varpi^{stable}|/\varpi^{stable}]$. Fig. 7a presents the log-relative error of the 4th- and 5th-order Gauss-Lobatto DQFE methods. For first-order frequency ϖ_1, the convergence (defined as a relative error under 1×10^{-6}) is achieved at 800 DOF (i.e., a 6×6 mesh grid for nine-node DQFE method). Additionally, Fig. 7b convergence rates $r = (\varpi_{k+1} - \varpi^*)/(\varpi_k - \varpi^*)$ using Navier-based analytical benchmarks, revealing the 5th-order nine-node DQFE exhibits accelerated convergence under identical DOFs, demonstrating computational superiority.

Table 1 The correspondence between mesh division and DOF of the two DQFEs

DOF	128	392	800	1352	2048	2888	3872	5000	6272	7688	9248	…
M	2	4	6	8	10	12	14	16	18	20	22	…
N	3	6	9	12	15	18	21	24	27	30	33	…

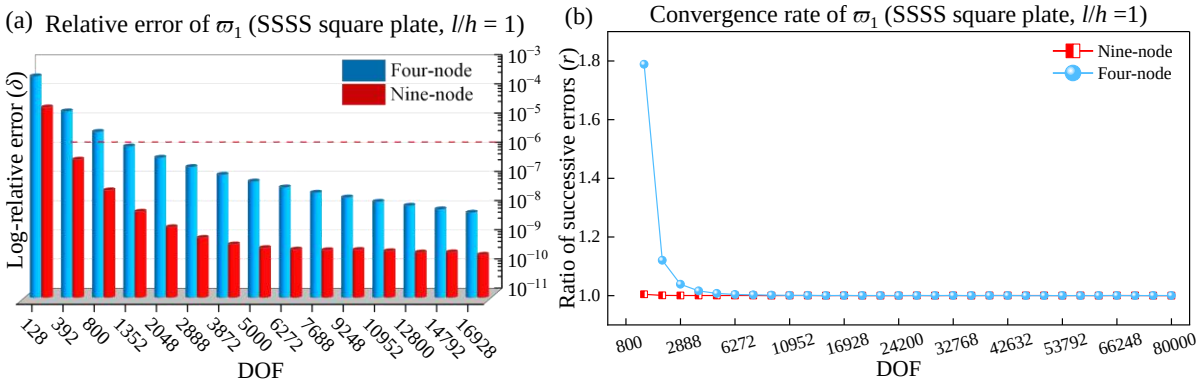

Fig. 7 Comparison of 1st-order frequency convergence for two DQFEs of SSSS square microplates

Table 2 presents a methodological comparison between TSDT, quasi-3D, and the proposed approach. Current results demonstrate strong consistency with TSDT-based solutions, preserving four-decimal-place accuracy. For a/h = 5 (thick microplate), the results show relatively good agreement with the quasi-3D method for the first four l/h values, although the concordance diminishes for the last two l/h values (0.8 and 1). Conversely, for a/h = 20 (moderately thick microplate) and a/h = 100 (thin microplate), our findings consistently align with the quasi-3D results across the range from l/h = 0 to l/h = 1.

Table 2 Comparison of dimensionless fundamental frequencies $\varpi = \frac{\omega a^2}{h}\sqrt{\frac{\rho}{E}}$ of SSSS homogeneous microplates

a/h	Theory	l/h					
		0	0.2	0.4	0.6	0.8	1
5	Present	5.2813	5.7699	7.0330	8.7389	10.6766	12.7408
	TSDT [78]	5.2813	5.7699	7.0330	8.7389	10.6766	12.7408
	Quasi-3D [79]	5.3090	5.7622	6.9438	8.5509	9.8943	9.9791
20	Present	5.9199	6.4027	7.6708	9.4116	11.4108	13.5545
	TSDT [78]	5.9199	6.4027	7.6708	9.4116	11.4108	13.5545
	Quasi-3D [79]	5.9235	6.4030	7.6633	9.3952	11.3854	13.5202
100	Present	5.9712	6.4535	7.7217	9.4651	11.4689	13.6186
	TSDT [78]	5.9712	6.4535	7.7217	9.4651	11.4689	13.6186
	Quasi-3D [79]	5.9723	6.4544	7.7222	9.4650	11.4683	13.6177

Table 3 summarizes the first five dimensionless frequencies predicted by the proposed HSDT-based DQFE methodology and the FSDT-based pb-2 Ritz approach [80-82] for macroscopic skew, isosceles trapezoidal, and annular sectorial plates, as shown in Figs. 5b-5d. Both methodologies demonstrate strong agreement in free vibration analyses across diverse boundary configurations. Minor discrepancies stemming from fundamental theoretical distinctions between the plate formulations were observed.

Table 3 Comparison of the present HSDT with the results from FSDT-based *pb*-2 Ritz method

BC	Method	ϖ_1	ϖ_2	ϖ_3	ϖ_4	ϖ_5
Skew plate ($\varpi = \left(\omega a^2/\pi^2\right)\Big/\sqrt{\rho h/D}$, h/a = 0.001, b/a = 1, β = 30°)						
SSSS	FSDT [80]	2.5294	5.3333	7.2821	8.4966	12.4442
	Present	2.5254	5.3333	7.2721	8.4948	12.4442
CCCC	FSDT [80]	4.6698	8.2677	10.6554	12.0825	16.7159
	Present	4.6698	8.2677	10.6554	12.0824	16.7159
Isosceles trapezoidal ($\varpi = \left(\omega a^2/2\pi\right)\Big/\sqrt{\rho h/D}$, h/b = 0.001, b/a = 1, c/a = 0.4)						
CFFF	FSDT [81]	0.7032	2.6518	3.6686	7.2957	9.6493
	Present	0.7036	2.6518	3.6684	7.2949	9.6482
SSSS	FSDT [81]	4.9015	10.1673	13.1935	18.0536	21.0193
	Present	4.9002	10.1621	13.1937	18.0452	21.0185
CCCC	FSDT	9.2239	15.5815	19.8875	24.5113	29.1914
	Present	9.2240	15.5816	19.8877	24.5106	29.1916
Annular sectorial plate ($\varpi = \omega R_2^2\Big/\sqrt{\rho h/D}$, h/R_2= 0.001, α = 0.5, β = 45°)						
SCSC	FSDT [82]	107.5627	178.8039	269.4713	305.6037	346.4505
	Present	108.1388	179.7046	270.0226	306.2127	347.3561
CSCS	FSDT [82]	92.8943	200.6703	206.1239	332.6893	347.5904
	Present	93.7850	201.9383	207.6771	334.2877	348.8583

Additionally, macroscopic cantilever plates with asymmetric trapezoidal shapes are considered, as shown in Fig. 8. Table 4 compares the first five natural frequencies predicted by the present method with experimental data and numerical results from Abaqus® [83], while Table 5 displays the corresponding mode shapes. The material properties used are E = 70 GPa, ν = 0.33, and ρ = 2800 kg/m^3. The vibration frequencies and mode shapes obtained from the present HSDT-based DQFE model are more consistent with experimental data compared to the Abaqus FE model [83].

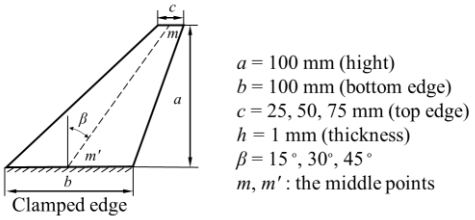

Fig. 8 Asymmetric trapezoidal cantilever plate configuration [83]

Table 4 Comparison of the first five natural frequencies (Hz) for cantilever trapezoidal plates

β	Mode order	c/b = 0.25			c/b = 0. 5			c/b = 0.75		
		Exp. [83]	FEM [83]	Present	Exp. [83]	FEM [83]	Present	Exp. [83]	FEM [83]	Present
15°	1	115	118	116	93	100	98	85	90	88
	2	464	478	468	333	346	340	243	259	254
	3	568	603	590	529	555	542	514	533	520
	4	1167	1214	1182	957	963	941	779	794	776
	5	1547	1590	1540	1387	1454	1416	1019	1039	1016
30°	1	98	105	105	82	88	87	74	79	77
	2	414	421	420	301	318	312	239	241	237
	3	584	603	601	514	527	515	487	494	482
	4	976	1029	1019	782	828	808	667	682	667
	5	1455	1562	1539	1338	1423	1376	1128	1157	1126
45°	1	73	79	78	63	66	65	55	58	57
	2	329	340	332	263	272	267	205	214	210
	3	515	542	531	420	446	436	388	399	390
	4	821	840	815	665	677	659	547	567	553
	5	1204	1272	1226	1106	1142	1103	963	984	954

Table 5 Comparison of the first five mode shapes of the cantilever trapezoidal plates with $\beta = 15°$, $c/b = 0.75$.

Method	Mode shape				
	1st	2nd	3rd	4th	5th
Present	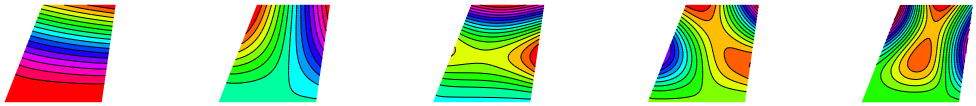				
Exp. [83]	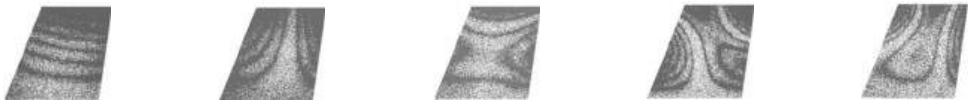				
FEM [83]	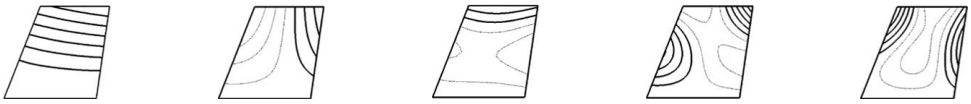				

4.2 *Cyclic quadrilateral microplates*

This subsection applies the developed DQFE to the transverse vibration analysis of cyclic quadrilateral plates. A circle with a radius R_0 contains an inscribed cyclic square with an area of A_0. By varying the central angle at one vertex of the square, a series of cyclic quadrilaterals with constant area can be generated based on the square inscribed in the circle. As depicted in Figs. 9a and 9b, the central angle (β, unit: °) of the 4th vertex ranges from 90° to 135°, while the area of the cyclic quadrilateral remains constant at A_0, achieved solely by adjusting the radius, as described by Eq. (46). The characteristic length is defined as the side length of the corresponding cyclic square area ($L_c = \sqrt{2}R$) and the dimensionless frequency is $\varpi = \omega L_c^2 \sqrt{\rho h / D}$.

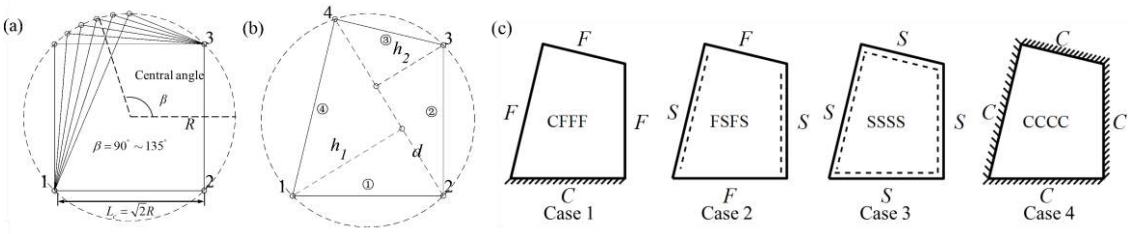

Fig. 9 Configurations of the cyclic quadrilateral plate and boundary conditions (F: free, C: clamp, S: simply supported)

$$A = \frac{1}{2} d\left(h_1 + h_2\right), \frac{A}{A_0} = \left(\frac{R}{R_0}\right)^2, R' = R_0 \sqrt{\frac{A_0}{A}} \tag{46}$$

Example 1. The influence of size-dependent effects, symbolized by MLSP, on the mode transitions of the cyclic quadrilateral microplate under four boundary conditions is investigated, as shown in Fig. 9c. Similarly, the mode transition phenomena have been reported in the buckling mode shapes [55]. In Figs. 10 and 11, the adjacent eigenmodes (4th–5th or 3rd–4th) for MSLP-to-thickness ratio l/h values of 0, 0.5, and 1, respectively, are compared. For a fixed l/h, the frequency-β curves of the adjacent modes converge toward each other, subsequently, swap trajectories, extend along each other's original paths, a phenomenon referred to as frequency loci veering [84], often accompanied by mode transition or the variation of modal localization. Overall, the dimensionless frequencies increase with increasing l/h.

Under weak boundary conditions, as shown in Fig. 10, the angle parameter corresponding to mode shape transition varies by increasing MLSP. One can see that MLSP has a dramatic effect on the mode shapes for CFFF and FSFS microplates. For the 4th and 5th frequencies of the CFFF plate, the mode transition angle decreases with increasing l/h, from 126° to 115.2° and 109.8°, respectively. When $l/h = 0.5$, the 4th and 5th mode shapes are interchanged. While $l/h = 1$, the mode shapes evolve from their original localization due to the combined influence of cantilever boundary condition, shear effect, and strong couple-stress effect rather than undergoing a simple mode transition. Boundary conditions govern a structure's constraints and deformation, directly influencing microplates' stiffness distribution and mode shapes. Because the cantilever

microplate has one side constrained, the stiffness near the clamped side is more significant than those of three free sides, causing larger deflections near the free sides. The stiffness is inversely proportional to the deflection. As a result, the vibrational behavior is dominated by the free-end region. Taking the shape close to a square as the reference, the 4th mode shape is primarily concentrated near side 3, with smaller concentrations near sides 2 and 4. The 5th mode shape exhibits four regions of concentrated vibration near sides 2, 3, and 4. As β decreases, side 3 shortens while side 4 elongates, resulting in a change in the stiffness distribution of the plate, which no longer maintains symmetry between the left and right sides. As MLSP (l) increases, the couple-stress effect becomes more pronounced, which does not contribute to the kinetic energy corresponding mass matrix. However, it increases the plate's stiffness, thereby increasing the vibration frequency, as can be seen from the coefficients in Eq (7). The enhanced couple-stress effect further alters this non-uniform distribution. In contrast to the macroscopic case, the size-dependent effect leads to mode localization, resulting in a higher proportion of the fourth-order mode. A larger reduction in β, i.e., an increase in shape asymmetry, is required to achieve a mode transition.

For FSFS, the mode shape variations appear disorganized. An increase in l/h results in a mode transition between the 3rd and 4th frequencies, accompanied by a decrease in the corresponding central angle. It is clear that the mode shapes have changed at the mode transition angle, but the two adjacent orders of mode shapes are not interchanged. As mentioned in CFFF, this boundary condition and the geometric parameter β influence the plate's stiffness distribution. For the 3rd-order mode shapes of the square plate with simply supported sides 1 and 3 and free sides 2 and 4, the mode shapes are symmetric and uniformly distributed about the free sides 2 and 4. The 4th-order mode shape is symmetric about the 1-3 pair sides, with the modal vibration primarily concentrated in the central region. As β decreases, the plate shape becomes irregular, leading to a non-uniform stiffness distribution and thus triggering a mode localization variation. Based on the characteristics of the mode shapes under FSFS, the couple-stress effect enhances the mode localization. Therefore, a further reduction in β is required to induce phenomena such as frequency loci veering or mode transitions.

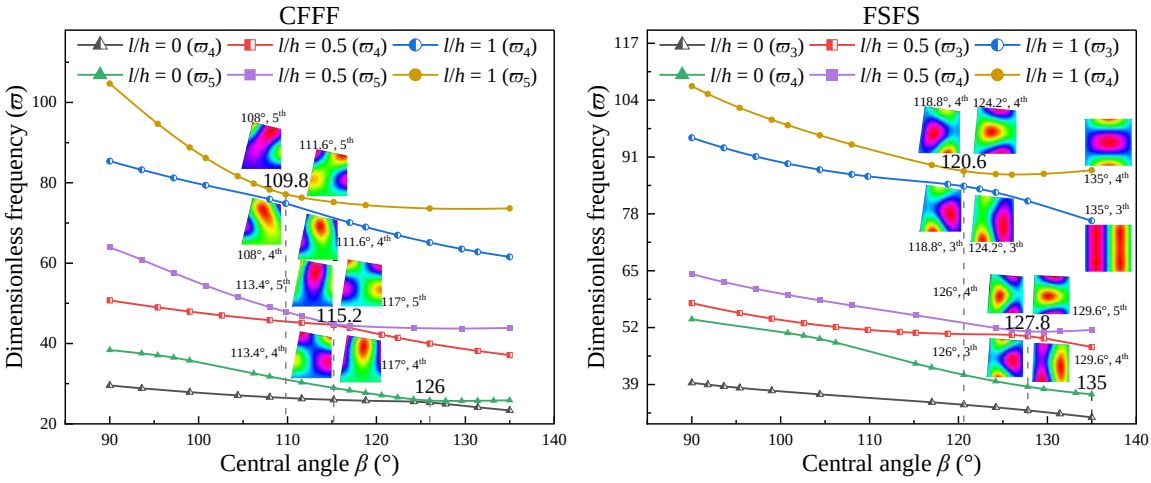

Fig. 10 Effect of MLSP on the vibration of CFFF and FSFS thick plates ($h/L_c = 0.2$)

As shown in Fig. 11, the dimensionless frequencies increase with the ratio l/h. However, as l/h increases from 0 to 1, the central angles of mode transitions for SSSS and CCCC remain nearly unchanged. Analysis reveals that when at least one boundary of the microplate is free, the central angle β corresponding to mode transitions is more likely to change with an increasing MLSP. In contrast, when all boundaries are simply supported or clamped, the mode transition angle remains nearly constant. This suggests that size-dependent effects generally manifest themselves in connection with boundary conditions. Stronger boundary constraints lead to a more stable central angle for mode transitions. When all four sides of the plate are constrained, the stiffness is predominantly concentrated near the sides, with the primary vibrational modes localized within the interior region of the plate, where the stiffness distribution remains relatively uniform. The couple-stress effect uniformly enhances the stiffness of the plate. Consequently, as the MLSP increases,

the β values associated with mode transitions for SSSS and CCCC plates remain consistent. This behavior occurs because the stiffness increase simultaneously affects all mode shapes, resulting in a proportional mode transition while preserving a consistent energy distribution across the modes.

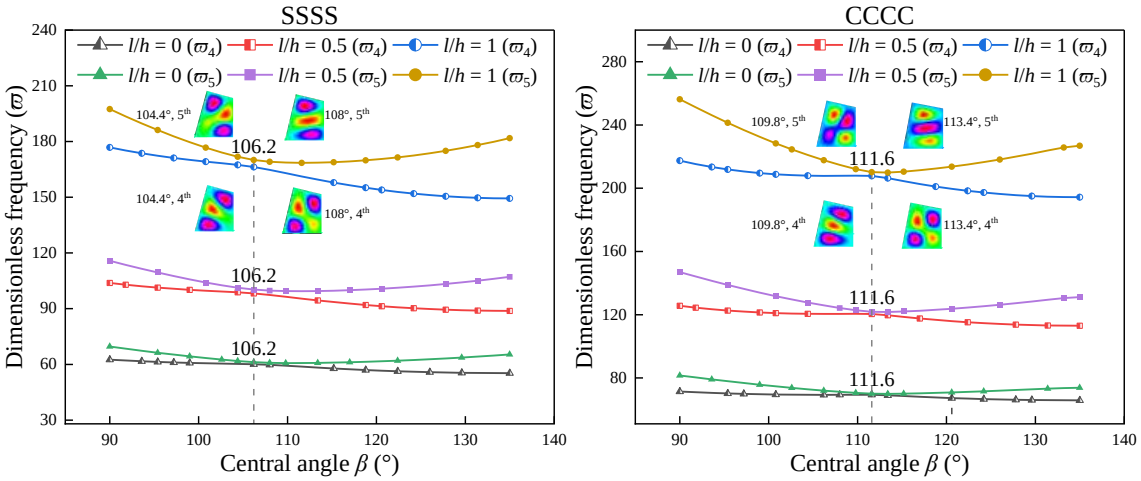

Fig. 11 Effect of MLSP on the vibration of SSSS and CCCC thick plates (h/L_c = 0.2)

Example 2. For simplicity, β is set to 100° based on the observed mode transition patterns. Table 6 presents the first five mode shapes for the cyclic quadrilateral microplates under various boundary conditions, namely CFFF and FSFS. The modal localization of the first five mode shapes is investigated. Likewise, Ref. [85] reported the modal localization phenomenon of the macroscopic multi-span bridge plates.

The mode assurance criterion (MAC), as defined in Eq. (47) is employed to assess the size-dependent modal localization by quantifying the correlation between two i^{th} modal vectors (P and Q) [86]. As shown in Fig. 12, as the ratio l/h increases, the 4th and 5th modes exhibit significant variations compared to the macroscale plate, particularly the 5th mode of the CFFF plate, with a correlation coefficient of 0.5257.

$$R_i = \left| \frac{n\left(P_i\right)^T Q_i - n^2 \bar{P}_i \bar{Q}_i}{\sqrt{\left(P_i\right)^T P_i - n^2 \bar{P}_i^2} \cdot \sqrt{\left(Q_i\right)^T Q_i - n^2 \bar{Q}_i^2}} \right| \tag{47}$$

Table 6 First five mode shapes of the CFFF cyclic quadrilateral thick plate (h/L_c = 0.2, β = 100°) under different l/h values

l/h	Mode shape				
	1st	2nd	3rd	4th	5th
0	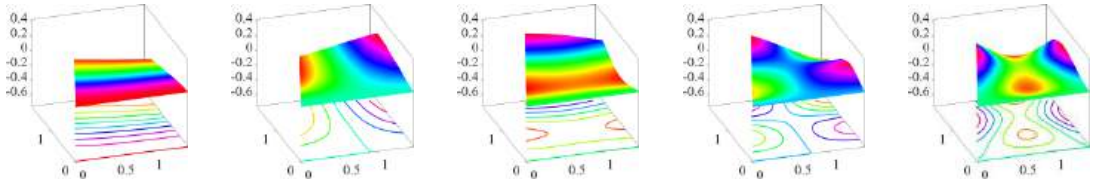				
0.5	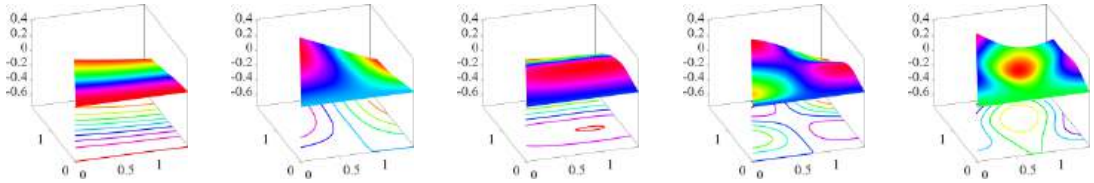				
1	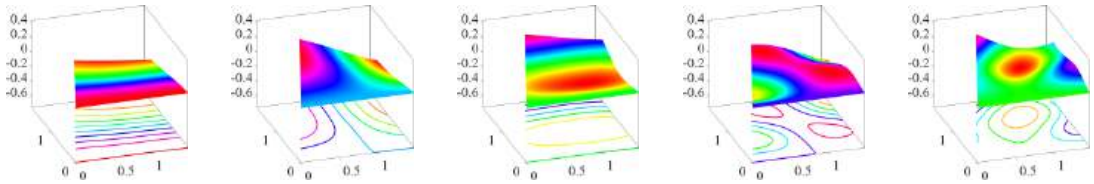				

Table 7 First five mode shapes of the FSFS cyclic quadrilateral thick plate ($h/L_c = 0.2$, $\beta = 100°$) under different l/h values

l/h	Mode shape				
	1st	2nd	3rd	4th	5th
0	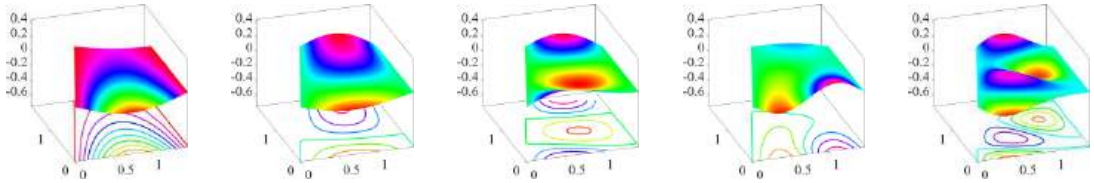				
0.5	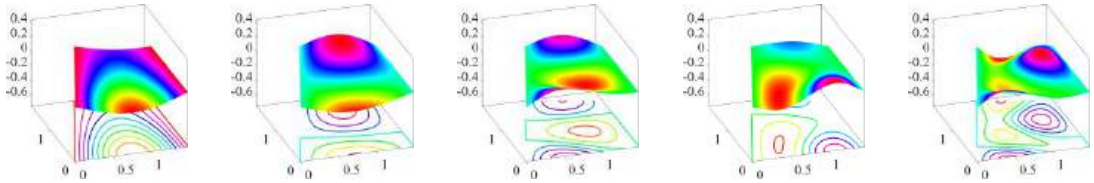				
1	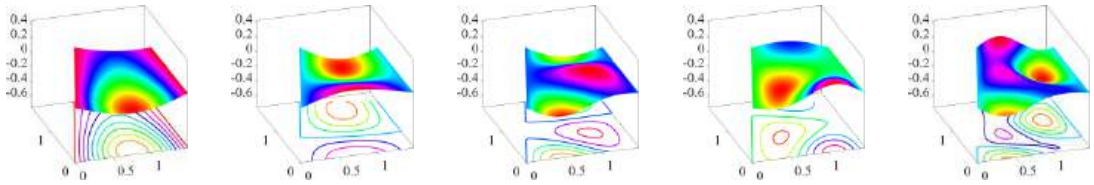				

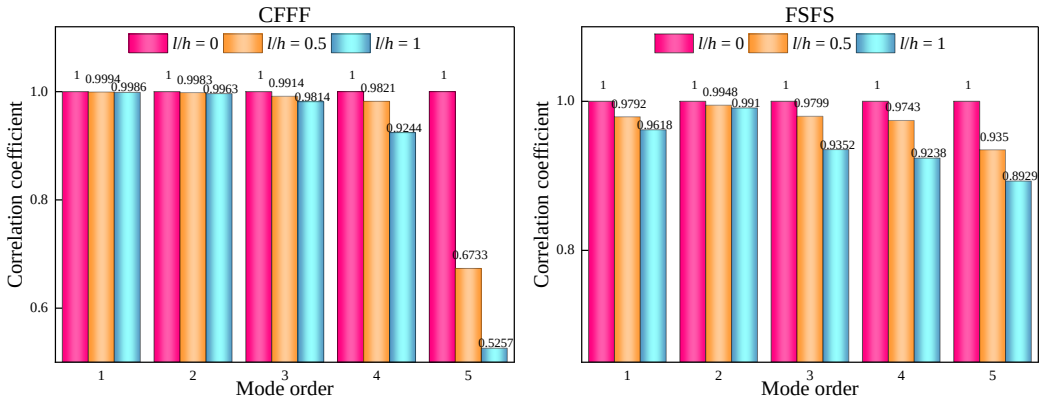

Fig. 12 Modal correlation coefficients for CFFF and FSFS cyclic quadrilateral thick plates ($h/L_c = 0.2$, $\beta = 100°$)

Example 3. This section analyzes the shear effects on the free vibration frequencies and mode shapes of the cyclic quadrilateral macro plate. The shear effects are isolated using the macroscopic plate, which eliminates the influence of the MLSP. The thickness-to-characteristic length h/L_c values of 0.001, 0.1, and 0.2 are considered for the CFFF boundary condition, with β set to 100°. The results in Fig. 13 reveal that higher-order modes are more significantly influenced by shear deformation, resulting in a more rapid decrease in frequency as the thickness increases. Specifically, for the CFFF plate, the frequencies of the 1st and 2nd modes exhibit minimal variation, while the higher-order mode frequencies decrease considerably.

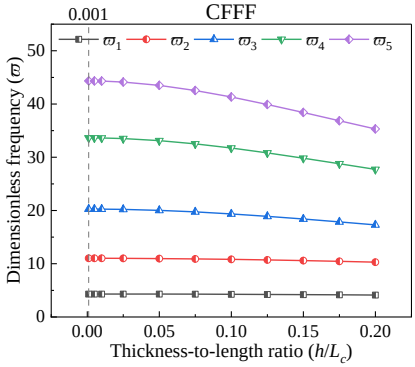

Fig. 13 Effect of h/L_c on the vibration frequencies of the cyclic quadrilateral plates ($\beta = 100°$, $l/h = 0$)

Three h/L_c ratios—0.001, 0.1, and 0.2—were analyzed to quantify the effect of shear deformation on

modal localization. As shown in Fig. 14 and Table 8, when the ratio is 0.2, the 5th mode of the CFFF plate exhibits a lower correlation.

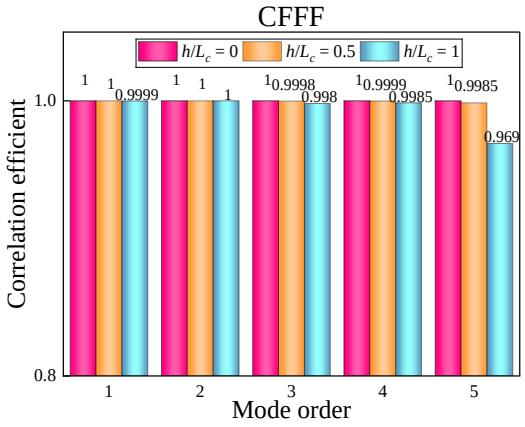

Fig. 14 Modal correlation coefficients of CFFF and SSCC cyclic quadrilateral plates ($l/h = 0$, $\beta = 100°$) with h/L_c

Table 8 First five mode shapes of CFFF cyclic quadrilateral plate ($l/h = 0$, $\beta = 100°$) under different h/L_c ratios

h/L_c	Mode shape				
	1st	2nd	3rd	4th	5th
0.001	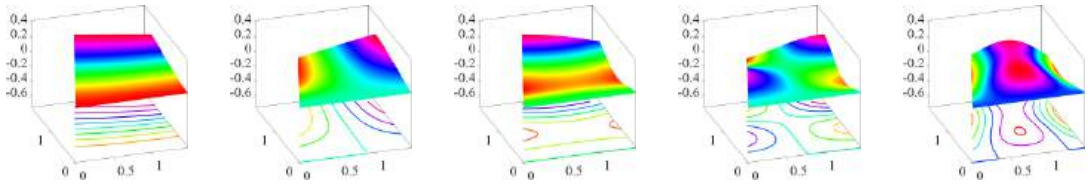				
0.1	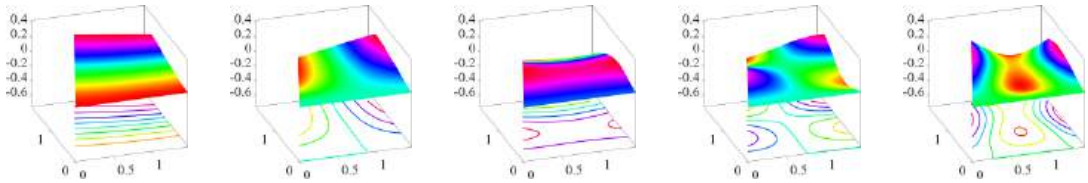				
0.2	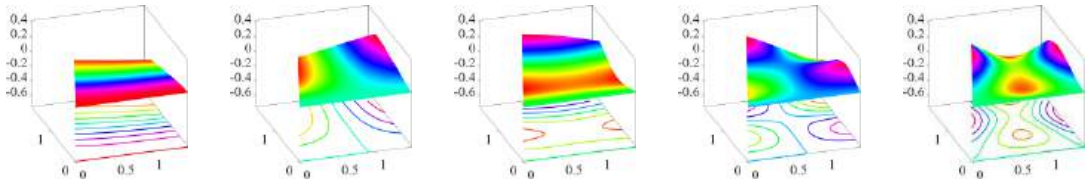				

5 Conclusions

The governing equations for freely vibrating quadrilateral microplates are established through the synergistic integration of modified couple stress theory (MCST) and a refined higher-order shear deformation theory (HSDT). A 50-DOF nine-node differential quadrature finite element (DQFE) is developed to resolve the resultant eighth-order boundary-value problem. The computational robustness of the proposed framework is rigorously verified through comparative analysis of free vibration frequencies across rectangular, skew, isosceles/asymmetric trapezoidal, and annular sectorial plates against benchmark solutions. Extending beyond conventional geometries, this investigation quantitatively explores dynamic responses of equal-area cyclic quadrilateral plates, elucidating mechanistic dependencies on material length scale parameter (MLSP) and thickness ratio through parametric studies. Advanced modal decomposition techniques reveal critical correlations between these parameters, mode shapes, and associated correlation coefficients. Four principal conclusions emerge:

(1) The nine-node DQFE demonstrates superior convergence characteristics compared to prior four-node implementations.

(2) Central angle variation governs frequency modulation in cyclic quadrilateral plates, driving intermodal transitions under invariant area constraints.

(3) Material size dependency critically governs modal localization phenomena, with marked correlation coefficient reduction (l/h = 1) observed in CFFF/FSFS configurations.

(4) MLSP predominantly dictates frequency distribution and mode contour evolution; the thickness-to-minimum dimension ratio exhibits a secondary influence on vibrational characteristics.

Acknowledgments

This work was supported by the Natural Science Foundation of Sichuan Province (No.23NSFSC0849) and the National Natural Science Foundation of China (Nos. 11602204, 12272064, and 12222209). We are grateful to M.S. Tao Deng of Southwest Jiaotong University and Dr. Yuhang Duan of City University of Hong Kong for their useful discussion. The authors express gratitude to all reviewers involved in the review process and to MJEditor (www.mjeditor.com) for providing English editing services during the preparation of this manuscript.

Appendix A

$$\beta_1=\frac{7\Sigma_6}{6}\left(\eta_{,x}^2+\eta_{,y}^2\right)\left(\xi_{,x}\eta_{,x}+\eta_{,y}\xi_{,y}\right),\ \beta_2=\frac{7\Sigma_6}{3}\left(\xi_{,x}^2+\xi_{,y}^2\right)\left(\eta_{,x}^2+\eta_{,y}^2\right),\ \beta_3=\frac{7\Sigma_6}{6}\left(\xi_{,x}^2+\xi_{,y}^2\right)\left(\xi_{,x}\eta_{,x}+\eta_{,y}\xi_{,y}\right),$$

$$\beta_4=4\Sigma_2\left(\xi_{,x}\eta_{,x}^3+\xi_{,y}\eta_{,y}^3\right)+\left(\frac{1}{42}\Sigma_3+2\Sigma_5+\frac{3\Sigma_6}{4}\right)\left(\eta_{,x}^2\eta_{,y}\xi_{,y}+\eta_{,y}^2\xi_{,x}\eta_{,x}\right),$$

$$\beta_5=\frac{7\Sigma_6}{12}\left(\left(\xi_{,x}-\xi_{,y}\right)\eta_{,x}+\left(\xi_{,x}+\xi_{,y}\right)\eta_{,y}\right)\left(\left(\xi_{,x}+\xi_{,y}\right)\eta_{,x}-\left(\xi_{,x}-\xi_{,y}\right)\eta_{,y}\right),$$

$$\beta_6=\frac{7\Sigma_6}{6}\left(\xi_{,x}^2+\xi_{,y}^2\right)\left(\xi_{,x}\eta_{,x}+\eta_{,y}\xi_{,y}\right),\ \beta_7=\frac{7\Sigma_6\left(\xi_{,x}^2+\xi_{,y}^2\right)^2}{12},$$

$$\beta_8=2\Sigma_2\left(\xi_{,x}^2\eta_{,x}^2+\xi_{,y}^2\eta_{,y}^2\right)+\left(\frac{1}{84}\Sigma_3-\frac{3}{8}\Sigma_6\right)\left(\xi_{,x}^2\eta_{,y}^2+\xi_{,y}^2\eta_{,x}^2\right)+2\left(\Sigma_5+\frac{3\Sigma_6}{4}\right)\xi_{,x}\xi_{,y}\eta_{,x}\eta_{,y},$$

$$\beta_9=4\Sigma_2\left(\xi_{,x}^3\eta_{,x}+\xi_{,y}^3\eta_{,y}\right)+\left(\frac{\Sigma_3}{42}+2\Sigma_5+\frac{63\Sigma_6}{84}\right)\left(\xi_{,x}^2\eta_{,y}\xi_{,y}+\xi_{,y}^2\eta_{,x}\xi_{,x}\right),$$

$$\beta_{10}=\Sigma_1\left(\eta_{,x}^4+\eta_{,y}^4\right)+\left(\Sigma_3+84\Sigma_5+\Sigma_6\right)\eta_{,x}^2\eta_{,y}^2,$$

$$\beta_{11}=\left(4\xi_{,x}^2\Sigma_1+84\xi_{,y}^2\left(\Sigma_5+\frac{\Sigma_6}{42}\right)\right)\eta_{,x}^2+4\left(\Sigma_3+42\Sigma_5\right)\xi_{,x}\xi_{,y}\eta_{,x}\eta_{,y}+84\left(\left(\Sigma_5+\frac{\Sigma_6}{42}\right)\xi_{,x}^2+\frac{\xi_{,y}^2\Sigma_1}{21}\right)\eta_{,y}^2,$$

$$\beta_{12}=\Sigma_1\xi_{,x}^4+\xi_{,y}^2\left(\Sigma_3+84\Sigma_5+\Sigma_6\right)\xi_{,x}^2+\Sigma_1\xi_{,y}^4,\ \beta_{13}=\Sigma_2\eta_{,x}^4+\frac{1}{84}\left(\Sigma_3+84\Sigma_5+\frac{63\Sigma_6}{2}\right)\eta_{,x}^2\eta_{,y}^2+\Sigma_2\eta_{,y}^4,$$

$$\beta_{14}=\left(4\xi_{,x}^2\Sigma_2+\xi_{,y}^2\left(\Sigma_5+\frac{3\Sigma_6}{4}\right)\right)\eta_{,x}^2+\frac{\left(\Sigma_3+42\Sigma_5\right)}{21}\xi_{,x}\xi_{,y}\eta_{,x}\eta_{,y}+\left(\left(\Sigma_5+\frac{3\Sigma_6}{4}\right)\xi_{,x}^2+4\xi_{,y}^2\Sigma_2\right)\eta_{,y}^2,$$

$$\beta_{15}=\Sigma_2\xi_{,x}^4+\frac{1}{84}\left(\Sigma_3+84\Sigma_5+\frac{63\Sigma_6}{2}\right)\xi_{,x}^2\xi_{,y}^2+\Sigma_2\xi_{,y}^4,$$

$$\beta_{16}=\left(2\xi_{,x}^2\Sigma_1+\xi_{,y}^2\left(\Sigma_3-\Sigma_6\right)\right)\eta_{,x}^2+168\left(\Sigma_5+\frac{\Sigma_6}{42}\right)\xi_{,x}\xi_{,y}\eta_{,x}\eta_{,y}+\left(\left(\Sigma_3-\Sigma_6\right)\xi_{,x}^2+2\xi_{,y}^2\Sigma_1\right)\eta_{,y}^2,$$

$$\beta_{17}=4\Sigma_1\xi_{,x}^3\eta_{,x}+2\left(\Sigma_3+84\Sigma_5+\Sigma_6\right)\xi_{,x}^2\xi_{,y}\eta_{,y}+2\left(\Sigma_3+84\Sigma_5+\Sigma_6\right)\xi_{,x}\xi_{,y}^2\eta_{,x}+4\Sigma_1\xi_{,y}^3\eta_{,y},$$

$$\beta_{18}=\frac{7\Sigma_6}{12}\left(\eta_{,x}^2+\eta_{,y}^2\right)^2,\beta_{19}=\frac{7\Sigma_6}{6}\left(\eta_{,x}^2+\eta_{,y}^2\right)\left(\xi_{,x}\eta_{,x}+\eta_{,y}\xi_{,y}\right),$$

$$\beta_{20}=\frac{7\Sigma_6}{12}\left(\left(\xi_{,x}+\xi_{,y}\right)\eta_{,x}-\eta_{,y}\left(\xi_{,x}-\xi_{,y}\right)\right)\left(\left(\xi_{,x}-\xi_{,y}\right)\eta_{,x}+\eta_{,y}\left(\xi_{,x}+\xi_{,y}\right)\right),$$

$$\beta_{21}=4\Sigma_1\xi_{,x}\eta_{,x}^3+2\left(\Sigma_3+84\Sigma_5+\Sigma_6\right)\xi_{,y}\eta_{,x}^2\eta_{,y}+2\left(\Sigma_3+84\Sigma_5+\Sigma_6\right)\xi_{,x}\eta_{,x}\eta_{,y}^2+4\Sigma_1\xi_{,y}\eta_{,y}^3,$$

$$\beta_{22}=\left(2\Sigma_1\xi_{,xx}+\Sigma_3\xi_{,yy}-\Sigma_6\xi_{,yy}\right)\eta_{,x}^2+168\left(\Sigma_5+\frac{\Sigma_6}{42}\right)\xi_{,xy}\eta_{,y}\eta_{,x}+\left(2\Sigma_1\xi_{,yy}+\Sigma_3\xi_{,xx}-\Sigma_6\xi_{,xx}\right)\eta_{,y}^2,$$

$$\beta_{23}=\frac{7\Sigma_6}{12}\left(\left(\eta_{,xx}-\eta_{,yy}\right)\eta_{,x}^2+4\eta_{,y}\eta_{,x}\eta_{,xy}-\left(\eta_{,xx}-\eta_{,yy}\right)\eta_{,y}^2\right),$$

$$\beta_{24}=\frac{7\Sigma_6}{6}\left(\left(2\xi_{,y}\eta_{,xy}+\left(\eta_{,xx}-\eta_{,yy}\right)\xi_{,x}\right)\eta_{,x}+\left(2\xi_{,x}\eta_{,xy}-\xi_{,y}\left(\eta_{,xx}-\eta_{,yy}\right)\right)\eta_{,y}\right),$$

$$\beta_{25}=\frac{7\Sigma_6}{12}\left(\left(\eta_{,xx}-\eta_{,yy}\right)\left(\xi_{,x}^2-\xi_{,y}^2\right)+4\xi_{,x}\xi_{,y}\eta_{,xy}\right),\ \beta_{26}=\frac{7\Sigma_6}{12}\left(\left(\xi_{,xx}-\xi_{,yy}\right)\left(\eta_{,x}^2-\eta_{,y}^2\right)+4\xi_{,xy}\eta_{,y}\eta_{,x}\right),$$

$$\beta_{27}=\frac{7\Sigma_6}{6}\left(\left(2\xi_{,y}\xi_{,xy}+\left(\xi_{,xx}-\xi_{,yy}\right)\xi_{,x}\right)\eta_{,x}+\left(2\xi_{,x}\xi_{,xy}-\xi_{,y}\left(\xi_{,xx}-\xi_{,yy}\right)\right)\eta_{,y}\right),$$

$$\beta_{28}=\frac{7\Sigma_6}{12}\left(\left(\xi_{,xx}-\xi_{,yy}\right)\xi_{,x}^2+4\xi_{,y}\xi_{,x}\xi_{,xy}-\xi_{,y}^2\left(\xi_{,xx}-\xi_{,yy}\right)\right),$$

$$\beta_{29}=\left(2\Sigma_2\xi_{,xx}+\frac{1}{84}\Sigma_3\xi_{,yy}-\frac{3}{8}\Sigma_6\xi_{,yy}\right)\eta_{,x}^2+2\left(\Sigma_5+\frac{3\Sigma_6}{4}\right)\xi_{,xy}\eta_{,y}\eta_{,x}+\left(2\Sigma_2\xi_{,yy}+\frac{1}{84}\Sigma_3\xi_{,xx}-\frac{3}{8}\Sigma_6\xi_{,xx}\right)\eta_{,y}^2,$$

$$\beta_{30}=\left(2\Sigma_1\eta_{,xx}+\Sigma_3\eta_{,yy}-\Sigma_6\eta_{,yy}\right)\eta_{,x}^2+168\left(\Sigma_5+\frac{\Sigma_6}{42}\right)\eta_{,xy}\eta_{,y}\eta_{,x}+\eta_{,y}^2\left(2\Sigma_1\eta_{,yy}+\Sigma_3\eta_{,xx}-\Sigma_6\eta_{,xx}\right),$$

$$\beta_{31}=\left(\left(4\Sigma_1\eta_{,xx}+2\Sigma_3\eta_{,yy}-2\Sigma_6\eta_{,yy}\right)\xi_{,x}+168\left(\Sigma_5+\frac{\Sigma_6}{42}\right)\xi_{,y}\eta_{,xy}\right)\eta_{,x}+$$
$$\left(\left(4\Sigma_1\eta_{,yy}+2\Sigma_3\eta_{,xx}-2\Sigma_6\eta_{,xx}\right)\xi_{,y}+168\left(\Sigma_5+\frac{\Sigma_6}{42}\right)\xi_{,x}\eta_{,xy}\right)\eta_{,y},$$

$$\beta_{32}=\left(\left(4\Sigma_1\xi_{,xx}+2\Sigma_3\xi_{,yy}-2\Sigma_6\xi_{,yy}\right)\xi_{,x}+168\left(\Sigma_5+\frac{\Sigma_6}{42}\right)\xi_{,y}\xi_{,xy}\right)\eta_{,x}+$$
$$\left(\left(4\Sigma_1\xi_{,yy}+2\Sigma_3\xi_{,xx}-2\Sigma_6\xi_{,xx}\right)\xi_{,y}+168\left(\Sigma_5+\frac{\Sigma_6}{42}\right)\xi_{,x}\xi_{,xy}\right)\eta_{,y},$$

$$\beta_{33}=\left(2\Sigma_1\eta_{,xx}+\Sigma_3\eta_{,yy}-\Sigma_6\eta_{,yy}\right)\xi_{,x}^2+168\left(\Sigma_5+\frac{\Sigma_6}{42}\right)\eta_{,xy}\xi_{,y}\xi_{,x}+\left(2\Sigma_1\eta_{,yy}+\Sigma_3\eta_{,xx}-\Sigma_6\eta_{,xx}\right)\xi_{,y}^2,$$

$$\beta_{34}=\left(2\Sigma_1\xi_{,xx}+\Sigma_3\xi_{,yy}-\Sigma_6\xi_{,yy}\right)\xi_{,x}^2+168\left(\Sigma_5+\frac{\Sigma_6}{42}\right)\xi_{,xy}\xi_{,y}\xi_{,x}+\left(2\Sigma_1\xi_{,yy}+\Sigma_3\xi_{,xx}-\Sigma_6\xi_{,xx}\right)\xi_{,y}^2,$$

$$\beta_{35}=\frac{7\Sigma_6}{12}\left(\left(\eta_{,xx}-\eta_{,yy}\right)\eta_{,x}^2+4\eta_{,y}\eta_{,x}\eta_{,xy}-\left(\eta_{,xx}-\eta_{,yy}\right)\eta_{,y}^2\right),$$

$$\beta_{36}=\frac{7\Sigma_6}{12}\left(\left(\xi_{,xx}-\xi_{,yy}\right)\eta_{,x}^2+4\xi_{,xy}\eta_{,y}\eta_{,x}-\left(\xi_{,xx}-\xi_{,yy}\right)\eta_{,y}^2\right),$$

$$\beta_{37}=\left(2\Sigma_2\eta_{,xx}+\frac{1}{84}\Sigma_3\eta_{,yy}-\frac{3}{8}\Sigma_6\eta_{,yy}\right)\eta_{,x}^2+2\left(\Sigma_5+\frac{3\Sigma_6}{4}\right)\eta_{,xy}\eta_{,y}\eta_{,x}+\left(2\eta_{,yy}\Sigma_2+\frac{1}{84}\Sigma_3\eta_{,xx}-\frac{3}{8}\Sigma_6\eta_{,xx}\right)\eta_{,y}^2,$$

$$\beta_{38}=\frac{7\Sigma_6}{6}\left(\left(2\xi_{,y}\eta_{,xy}+\left(\eta_{,xx}-\eta_{,yy}\right)\xi_{,x}\right)\eta_{,x}+\left(2\xi_{,x}\eta_{,xy}-\xi_{,y}\left(\eta_{,xx}-\eta_{,yy}\right)\right)\eta_{,y}\right),$$

$$\beta_{39}=\frac{7\Sigma_6}{6}\left(\left(2\xi_{,y}\xi_{,xy}+\left(\xi_{,xx}-\xi_{,yy}\right)\xi_{,x}\right)\eta_{,x}+\left(2\xi_{,x}\xi_{,xy}-\xi_{,y}\left(\xi_{,xx}-\xi_{,yy}\right)\right)\eta_{,y}\right),$$

$$\beta_{40}=\frac{3}{2}\left(\left(\frac{1}{63}\Sigma_3\eta_{,yy}+\frac{8}{3}\Sigma_2\eta_{,xx}-\frac{1}{2}\Sigma_6\eta_{,yy}\right)\xi_{,x}+\left(\Sigma_6+\frac{4\Sigma_5}{3}\right)\xi_{,y}\eta_{,xy}\right)\eta_{,x}+$$
$$\frac{3}{2}\left(\left(\frac{1}{63}\Sigma_3\eta_{,xx}+\frac{8}{3}\Sigma_2\eta_{,yy}-\frac{1}{2}\Sigma_6\eta_{,xx}\right)\xi_{,y}+\left(\Sigma_6+\frac{4\Sigma_5}{3}\right)\xi_{,x}\eta_{,xy}\right)\eta_{,y},$$

$$\beta_{41}=\frac{3}{2}\left(\left(\frac{1}{63}\Sigma_3\xi_{,yy}+\frac{8}{3}\Sigma_2\xi_{,xx}-\frac{1}{2}\Sigma_6\xi_{,yy}\right)\xi_{,x}+\left(\Sigma_6+\frac{4\Sigma_5}{3}\right)\xi_{,y}\xi_{,xy}\right)\eta_{,x}+$$
$$\frac{3}{2}\left(\left(\frac{1}{63}\Sigma_3\xi_{,xx}+\frac{8}{3}\Sigma_2\xi_{,yy}-\frac{1}{2}\Sigma_6\xi_{,xx}\right)\xi_{,y}+\left(\Sigma_6+\frac{4\Sigma_5}{3}\right)\xi_{,x}\xi_{,xy}\right)\eta_{,y},$$

$$\beta_{42}=\frac{7\Sigma_6}{12}\left(\left(\eta_{,xx}-\eta_{,yy}\right)\xi_{,x}^2+4\xi_{,y}\xi_{,x}\eta_{,xy}-\xi_{,y}^2\left(\eta_{,xx}-\eta_{,yy}\right)\right),$$

$$\beta_{43}=\frac{7\Sigma_6}{12}\left(\left(\xi_{,xx}-\xi_{,yy}\right)\xi_{,x}^2+4\xi_{,y}\xi_{,x}\xi_{,xy}-\xi_{,y}^2\left(\xi_{,xx}-\xi_{,yy}\right)\right),$$

$$\beta_{44}=\left(2\Sigma_2\eta_{,xx}+\frac{1}{84}\Sigma_3\eta_{,yy}-\frac{3}{8}\Sigma_6\eta_{,yy}\right)\xi_{,x}^2+2\left(\Sigma_5+\frac{3\Sigma_6}{4}\right)\xi_{,x}\xi_{,y}\eta_{,xy}+\left(2\Sigma_2\eta_{,yy}+\frac{1}{84}\Sigma_3\eta_{,xx}-\frac{3}{8}\Sigma_6\eta_{,xx}\right)\xi_{,y}^2,$$

$$\beta_{45}=\left(2\Sigma_2\xi_{,xx}+\frac{1}{84}\Sigma_3\xi_{,yy}-\frac{3}{8}\Sigma_6\xi_{,yy}\right)\xi_{,x}^2+2\left(\Sigma_5+\frac{3\Sigma_6}{4}\right)\xi_{,x}\xi_{,y}\xi_{,xy}+\left(2\xi_{,yy}\Sigma_2+\frac{1}{84}\Sigma_3\xi_{,xx}-\frac{3}{8}\Sigma_6\xi_{,xx}\right)\xi_{,y}^2,$$

$$\beta_{46}=\Sigma_1\eta_{,xx}^2+\eta_{,yy}\left(\Sigma_3-\Sigma_6\right)\eta_{,xx}+\Sigma_1\eta_{,yy}^2+84\left(\Sigma_5+\frac{\Sigma_6}{42}\right)\eta_{,xy}^2,$$

$$\beta_{47}=\Sigma_1\xi_{,xx}^2+\xi_{,yy}\left(\Sigma_3-\Sigma_6\right)\xi_{,xx}+\Sigma_1\xi_{,yy}^2+84\left(\Sigma_5+\frac{\Sigma_6}{42}\right)\xi_{,xy}^2,$$

$$\beta_{48}=\Sigma_2\eta_{,xx}^2-\frac{3}{8}\left(\Sigma_6-\frac{2\Sigma_3}{63}\right)\eta_{,yy}\eta_{,xx}+\Sigma_2\eta_{,yy}^2+\Sigma_4\left(\eta_{,x}^2+\eta_{,y}^2\right)+\frac{3}{4}\left(\Sigma_6+\frac{4\Sigma_5}{3}\right)\eta_{,xy}^2,$$

$$\beta_{49}=\Sigma_2\xi_{,xx}^2-\frac{3}{8}\left(\Sigma_6-\frac{2\Sigma_3}{63}\right)\xi_{,yy}\xi_{,xx}+\Sigma_2\xi_{,yy}^2+\Sigma_4\left(\xi_{,x}^2+\xi_{,y}^2\right)+\frac{3}{4}\left(\Sigma_6+\frac{4\Sigma_5}{3}\right)\xi_{,xy}^2,$$

$$\beta_{50}=\left(4\eta_{,xy}\xi_{,xy}-\eta_{,xx}\xi_{,yy}-\eta_{,yy}\xi_{,xx}\right)\Sigma_6+\left(2\Sigma_1\xi_{,xx}+\Sigma_3\xi_{,yy}\right)\eta_{,xx}+\left(2\Sigma_1\xi_{,yy}+\Sigma_3\xi_{,xx}\right)\eta_{,yy}+168\Sigma_5\xi_{,xy}\eta_{,xy},$$

$$\beta_{51}=\frac{7\Sigma_6}{12}\left(\eta_{,xx}^2-2\eta_{,xx}\eta_{,yy}+4\eta_{,xy}^2+\eta_{,yy}^2\right),\ \beta_{52}=\frac{7\Sigma_6}{12}\left(\left(\xi_{,xx}-\xi_{,yy}\right)\eta_{,xx}+\left(-\xi_{,xx}+\xi_{,yy}\right)\eta_{,yy}+4\eta_{,xy}\xi_{,xy}\right),$$

$$\beta_{53}=\frac{7\Sigma_6}{12}\left(\left(\xi_{,xx}-\xi_{,yy}\right)\eta_{,xx}+\left(-\xi_{,xx}+\xi_{,yy}\right)\eta_{,yy}+4\eta_{,xy}\xi_{,xy}\right),\beta_{54}=\frac{7\Sigma_6}{12}\left(\xi_{,xx}^2-2\xi_{,xx}\xi_{,yy}+4\xi_{,xy}^2+\xi_{,yy}^2\right),$$

$$\beta_{55}=\frac{\left(2\Sigma_3-63\Sigma_6\right)}{168}\left(\xi_{,xx}\eta_{,yy}+\xi_{,yy}\eta_{,xx}\right)+2\Sigma_2\left(\xi_{,xx}\eta_{,xx}+\xi_{,yy}\eta_{,yy}\right)+2\Sigma_4\left(\xi_{,x}\eta_{,x}+\eta_{,y}\xi_{,y}\right)+2\Sigma_5\xi_{,xy}\eta_{,xy}+\frac{3}{2}\Sigma_6\xi_{,xy}\eta_{,xy}$$

Appendix B

$\boldsymbol{B}=\left[\boldsymbol{B}(1:25,1:13),\boldsymbol{B}(1:25,14:25)\right]$

$$\boldsymbol{B}(1:25,1:13)=\begin{bmatrix}
1 & 0 & 0 & 0 & 0 & 0 & 0 & 0 & 0 & 0 & 0 & 0 & 0\\
-p_1 & p_{11} & -p_4 & p_{10} & -p_2 & 0 & 0 & 0 & 0 & 0 & 0 & 0 & 0\\
-p_1 & 0 & 0 & 0 & 0 & p_{11} & 0 & 0 & 0 & 0 & -p_4 & 0 & 0\\
p_1^2 & -p_1p_{11} & p_1p_4 & -p_1p_{10} & p_1p_2 & -p_1p_{11} & p_{11}^2 & -p_4p_{11} & p_{10}p_{11} & -p_2p_{11} & p_1p_4 & -p_4p_{11} & p_4^2\\
0 & 0 & 1 & 0 & 0 & 0 & 0 & 0 & 0 & 0 & 0 & 0 & 0\\
0 & 0 & -p_1 & 0 & 0 & 0 & 0 & p_{11} & 0 & 0 & 0 & 0 & -p_4\\
0 & 0 & 0 & 0 & 1 & 0 & 0 & 0 & 0 & 0 & 0 & 0 & 0\\
p_2 & -p_{10} & p_4 & -p_{11} & p_1 & 0 & 0 & 0 & 0 & 0 & 0 & 0 & 0\\
0 & 0 & 0 & 0 & -p_1 & 0 & 0 & 0 & 0 & p_{11} & 0 & 0 & 0\\
-p_1p_2 & p_1p_{10} & -p_1p_4 & p_1p_{11} & -p_1^2 & p_2p_{11} & -p_{10}p_{11} & p_4p_{11} & -p_{11}^2 & p_1p_{11} & -p_2p_4 & p_{10}p_4 & -p_4^2\\
0 & 0 & 0 & 0 & 0 & 0 & 0 & 0 & 0 & 0 & 0 & 0 & 0\\
0 & 0 & 0 & 0 & 0 & 0 & 0 & 0 & 0 & 0 & p_2 & -p_{10} & p_4\\
0 & 0 & 0 & 0 & 0 & 0 & 0 & 0 & 0 & 0 & 0 & 0 & 0\\
0 & 0 & 0 & 0 & 0 & 0 & 0 & 0 & 0 & 0 & 0 & 0 & 0\\
0 & 0 & 0 & 0 & p_2 & 0 & 0 & 0 & 0 & -p_{10} & 0 & 0 & 0\\
p_2^2 & -p_2p_{10} & p_2p_4 & -p_2p_{11} & p_1p_2 & -p_2p_{10} & p_{10}^2 & -p_{10}p_4 & p_{10}p_{11} & -p_1p_{10} & p_2p_4 & -p_{10}p_4 & p_4^2\\
0 & 0 & 0 & 0 & 0 & 0 & 0 & 0 & 0 & 0 & 0 & 0 & 0\\
0 & 0 & p_2 & 0 & 0 & 0 & 0 & -p_{10} & 0 & 0 & 0 & 0 & p_4\\
0 & 0 & 0 & 0 & 0 & 0 & 0 & 0 & 0 & 0 & 0 & 0 & 0\\
0 & 0 & 0 & 0 & 0 & 0 & 0 & 0 & 0 & 0 & 0 & 0 & 0\\
p_2 & 0 & 0 & 0 & 0 & -p_{10} & 0 & 0 & 0 & 0 & p_4 & 0 & 0\\
-p_1p_2 & p_2p_{11} & -p_2p_4 & p_2p_{10} & -p_2^2 & p_1p_{10} & -p_{10}p_{11} & p_{10}p_4 & -p_{10}^2 & p_2p_{10} & -p_1p_4 & p_4p_{11} & -p_4^2\\
0 & 0 & 0 & 0 & 0 & 0 & 0 & 0 & 0 & 0 & 1 & 0 & 0\\
0 & 0 & 0 & 0 & 0 & 0 & 0 & 0 & 0 & 0 & -p_1 & p_{11} & -p_4\\
0 & 0 & 0 & 0 & 0 & 0 & 0 & 0 & 0 & 0 & 0 & 0 & 1
\end{bmatrix}$$

$$\boldsymbol{B}(1:25,14:25)=\begin{bmatrix}
0 & 0 & 0 & 0 & 0 & 0 & 0 & 0 & 0 & 0 & 0 & 0\\
0 & 0 & 0 & 0 & 0 & 0 & 0 & 0 & 0 & 0 & 0 & 0\\
0 & 0 & p_{10} & 0 & 0 & 0 & 0 & -p_2 & 0 & 0 & 0 & 0\\
-p_{10}p_4 & p_2p_4 & -p_1p_{10} & p_{10}p_{11} & -p_{10}p_4 & p_{10}^2 & -p_2p_{10} & p_1p_2 & -p_2p_{11} & p_2p_4 & -p_2p_{10} & p_2^2\\
0 & 0 & 0 & 0 & 0 & 0 & 0 & 0 & 0 & 0 & 0 & 0\\
0 & 0 & 0 & 0 & p_{10} & 0 & 0 & 0 & 0 & -p_2 & 0 & 0\\
0 & 0 & 0 & 0 & 0 & 0 & 0 & 0 & 0 & 0 & 0 & 0\\
0 & 0 & 0 & 0 & 0 & 0 & 0 & 0 & 0 & 0 & 0 & 0\\
0 & -p_4 & 0 & 0 & 0 & 0 & p_{10} & 0 & 0 & 0 & 0 & -p_2\\
p_4p_{11} & -p_1p_4 & p_2p_{10} & -p_{10}^2 & p_{10}p_4 & -p_{10}p_{11} & p_1p_{10} & -p_2^2 & p_2p_{10} & -p_2p_4 & p_2p_{11} & -p_1p_2\\
0 & 1 & 0 & 0 & 0 & 0 & 0 & 0 & 0 & 0 & 0 & 0\\
-p_{11} & p_1 & 0 & 0 & 0 & 0 & 0 & 0 & 0 & 0 & 0 & 0\\
0 & 0 & 0 & 0 & 0 & 0 & 0 & 0 & 0 & 0 & 0 & 1\\
0 & 0 & 0 & 0 & 0 & 0 & 0 & p_2 & -p_{10} & p_4 & -p_{11} & p_1\\
0 & p_4 & 0 & 0 & 0 & 0 & -p_{11} & 0 & 0 & 0 & 0 & p_1\\
-p_4p_{11} & p_1p_4 & -p_2p_{11} & p_{10}p_{11} & -p_4p_{11} & p_{11}^2 & -p_1p_{11} & p_1p_2 & -p_1p_{10} & p_1p_4 & -p_1p_{11} & p_1^2\\
0 & 0 & 0 & 0 & 0 & 0 & 0 & 0 & 0 & 1 & 0 & 0\\
0 & 0 & 0 & 0 & -p_{11} & 0 & 0 & 0 & 0 & p_1 & 0 & 0\\
0 & 0 & 0 & 0 & 0 & 0 & 0 & 1 & 0 & 0 & 0 & 0\\
0 & 0 & 0 & 0 & 0 & 0 & 0 & -p_1 & p_{11} & -p_4 & p_{10} & -p_2\\
0 & 0 & -p_{11} & 0 & 0 & 0 & 0 & p_1 & 0 & 0 & 0 & 0\\
p_{10}p_4 & -p_2p_4 & p_1p_{11} & -p_{11}^2 & p_4p_{11} & -p_{10}p_{11} & p_2p_{11} & -p_1^2 & p_1p_{11} & -p_1p_4 & p_1p_{10} & -p_1p_2\\
0 & 0 & 0 & 0 & 0 & 0 & 0 & 0 & 0 & 0 & 0 & 0\\
p_{10} & -p_2 & 0 & 0 & 0 & 0 & 0 & 0 & 0 & 0 & 0 & 0\\
0 & 0 & 0 & 0 & 0 & 0 & 0 & 0 & 0 & 0 & 0 & 0
\end{bmatrix}$$

where the independent coefficients are as follows: $p_1=5$, $p_2=\frac{1}{2}$, $p_3=\frac{3}{8}$, $p_4=\frac{8}{3}$, $p_5=\frac{\sqrt{21}}{6}$, $p_6=\frac{7\sqrt{21}}{24}$, $p_7=\frac{8\sqrt{21}}{21}$, $p_8=\frac{3}{4}-\frac{3\sqrt{21}}{28}$, $p_9=\frac{3}{4}+\frac{3\sqrt{21}}{28}$, $p_{10}=\frac{49}{12}-\frac{7\sqrt{21}}{12}$, $p_{11}=\frac{49}{12}+\frac{7\sqrt{21}}{12}$.

Appendix C

$$11:\begin{cases}\Delta_{11}=\Delta_{11}\\ \Delta_{,\xi}\big|_{11}=\Delta_{,x}\big|_{11}x_{,\xi}\big|_{11}+\Delta_{,y}\big|_{11}y_{,\xi}\big|_{11}\\ \Delta_{,\eta}\big|_{11}=\Delta_{,x}\big|_{11}x_{,\eta}\big|_{11}+\Delta_{,y}\big|_{11}y_{,\eta}\big|_{11}\\ \Delta_{,\xi\eta}\big|_{11}=x_{,\eta}\big|_{11}x_{,\xi}\big|_{11}\Delta_{,xx}\big|_{11}+y_{,\eta}\big|_{11}y_{,\xi}\big|_{11}\Delta_{,yy}\big|_{11}+\left(x_{,\eta}\big|_{11}y_{,\xi}\big|_{11}+x_{,\xi}\big|_{11}y_{,\eta}\big|_{11}\right)\Delta_{,xy}\big|_{11}+\\ \qquad\Delta_{,x}\big|_{11}x_{,\xi\eta}\big|_{11}+\Delta_{,y}\big|_{11}y_{,\xi\eta}\big|_{11}\end{cases}$$

$$31:\begin{cases}\Delta_{31}=\Delta_{31}\\ \Delta_{,\eta}\big|_{31}=\left[2\Delta_{,n}\big|_{31}|\mathbf{J}|_{31}-\left(\Delta_{51}-\Delta_{11}\right)\left(y_{,\eta}\big|_{31}n_x\big|_{31}-x_{,\eta}\big|_{31}n_y\big|_{31}\right)\right]\Big/2\left(x_{,\xi}\big|_{31}n_y\big|_{31}-y_{,\xi}\big|_{31}n_x\big|_{31}\right)\end{cases}$$

$$51:\begin{cases}\Delta_{51}=\Delta_{51}\\ \Delta_{,\xi}\big|_{51}=\Delta_{,x}\big|_{51}x_{,\xi}\big|_{51}+\Delta_{,y}\big|_{51}y_{,\xi}\big|_{51}\\ \Delta_{,\eta}\big|_{51}=\Delta_{,x}\big|_{51}x_{,\eta}\big|_{51}+\Delta_{,y}\big|_{51}y_{,\eta}\big|_{51}\\ \Delta_{,\xi\eta}\big|_{51}=x_{,\eta}\big|_{51}x_{,\xi}\big|_{51}\Delta_{,xx}\big|_{51}+y_{,\eta}\big|_{51}y_{,\xi}\big|_{51}\Delta_{,yy}\big|_{51}+\left(x_{,\eta}\big|_{51}y_{,\xi}\big|_{51}+x_{,\xi}\big|_{51}y_{,\eta}\big|_{51}\right)\Delta_{,xy}\big|_{51}+\\ \qquad\Delta_{,x}\big|_{51}x_{,\xi\eta}\big|_{51}+\Delta_{,y}\big|_{51}y_{,\xi\eta}\big|_{51}\end{cases}$$

$$53:\begin{cases}\Delta_{53}=\Delta_{53}\\ \Delta_{,\xi}\big|_{53}=\left[2\Delta_{,n}\big|_{53}|\mathbf{J}|_{53}-\left(\Delta_{55}-\Delta_{51}\right)\left(x_{,\xi}\big|_{53}n_y\big|_{53}-y_{,\xi}\big|_{53}n_x\big|_{53}\right)\right]\Big/2\left(y_{,\eta}\big|_{53}n_x\big|_{53}-x_{,\eta}\big|_{53}n_y\big|_{53}\right)\end{cases}$$

$$55:\begin{cases}\Delta_{55}=\Delta_{55}\\ \Delta_{,\xi}\big|_{55}=\Delta_{,x}\big|_{55}x_{,\xi}\big|_{55}+\Delta_{,y}\big|_{55}y_{,\xi}\big|_{55}\\ \Delta_{,\eta}\big|_{55}=\Delta_{,x}\big|_{55}x_{,\eta}\big|_{55}+\Delta_{,y}\big|_{55}y_{,\eta}\big|_{55}\\ \Delta_{,\xi\eta}\big|_{55}=x_{,\eta}\big|_{55}x_{,\xi}\big|_{55}\Delta_{,xx}\big|_{55}+y_{,\eta}\big|_{55}y_{,\xi}\big|_{55}\Delta_{,yy}\big|_{55}+\left(x_{,\eta}\big|_{55}y_{,\xi}\big|_{55}+x_{,\xi}\big|_{55}y_{,\eta}\big|_{55}\right)\Delta_{,xy}\big|_{55}+\\ \qquad\Delta_{,x}\big|_{55}x_{,\xi\eta}\big|_{55}+\Delta_{,y}\big|_{55}y_{,\xi\eta}\big|_{55}\end{cases}$$

$$35:\begin{cases}\Delta_{35}=\Delta_{35}\\ \Delta_{,\eta}\big|_{35}=\left[2\Delta_{,n}\big|_{35}|\mathrm{J}|_{35}-\left(\Delta_{51}-\Delta_{11}\right)\left(y_{,\eta}\big|_{35}n_x\big|_{35}-x_{,\eta}\big|_{35}n_y\big|_{35}\right)\right]\Big/2\left(x_{,\xi}\big|_{35}n_y\big|_{35}-y_{,\xi}\big|_{35}n_x\big|_{35}\right)\end{cases}$$

$$15:\begin{cases}\Delta_{15}=\Delta_{15}\\ \Delta_{,\xi}\big|_{15}=\Delta_{,x}\big|_{15}x_{,\xi}\big|_{15}+\Delta_{,y}\big|_{15}y_{,\xi}\big|_{15}\\ \Delta_{,\eta}\big|_{15}=\Delta_{,x}\big|_{15}x_{,\eta}\big|_{15}+\Delta_{,y}\big|_{15}y_{,\eta}\big|_{15}\\ \Delta_{,\xi\eta}\big|_{15}=x_{,\eta}\big|_{15}x_{,\xi}\big|_{15}\Delta_{,xx}\big|_{15}+y_{,\eta}\big|_{15}y_{,\xi}\big|_{15}\Delta_{,yy}\big|_{15}+\left(x_{,\eta}\big|_{15}y_{,\xi}\big|_{15}+x_{,\xi}\big|_{15}y_{,\eta}\big|_{15}\right)\Delta_{,xy}\big|_{15}+\\ \qquad\Delta_{,x}\big|_{15}x_{,\xi\eta}\big|_{15}+\Delta_{,y}\big|_{15}y_{,\xi\eta}\big|_{15}\end{cases}$$

$$13:\begin{cases}\Delta_{13}=\Delta_{13}\\ \Delta_{,\xi}\big|_{13}=\left[2\Delta_{,n}\big|_{13}|\mathrm{J}|_{13}-\left(\Delta_{55}-\Delta_{51}\right)\left(x_{,\xi}\big|_{13}n_y\big|_{13}-y_{,\xi}\big|_{13}n_x\big|_{13}\right)\right]/2\left(y_{,\eta}\big|_{13}n_x\big|_{13}-x_{,\eta}\big|_{13}n_y\big|_{13}\right)\end{cases}$$

$$33:\Delta_{33}=\Delta_{33}$$

Reference

[1] Wang B, Zhang B, Wu X, Zhou Y, Xiao L, Jiang S, et al. Design criteria for conformal integration of flexible

electronics on advanced aircraft surfaces. International Journal of Mechanical Sciences 2024;277: 109448.
[2] Zeng C, Hou S, Zhang H, Ou J. Dynamic plastic hinge rotation measurement for RC columns under seismic loads using MEMS inclinometers. Engineering Structures 2024;303: 117520.
[3] Gill WA, Howard I, Mazhar I, McKee K. A Review of MEMS Vibrating Gyroscopes and Their Reliability Issues in Harsh Environments. Sensors 2022;22(19).
[4] Qu J, Cui G, Li Z, Fang S, Zhang X, Liu A, et al. Advanced Flexible Sensing Technologies for Soft Robots. Advanced Functional Materials 2024;34(29): 2401311.
[5] Zhu J, Liu X, Shi Q, He T, Sun Z, Guo X, et al. Development Trends and Perspectives of Future Sensors and MEMS/NEMS. Micromachines 2020;11(1): 7.
[6] Setiono A, Bertke M, Nyang'au WO, Xu J, Fahrbach M, Kirsch I, et al. In-Plane and Out-of-Plane MEMS Piezoresistive Cantilever Sensors for Nanoparticle Mass Detection. Sensors 2020;20(3).
[7] Shaat M, Ghavanloo E, Fazelzadeh SA. Review on nonlocal continuum mechanics: Physics, material applicability, and mathematics. Mechanics of Materials 2020;150: 103587.
[8] Eringen AC. Theory of Nonlocal Elasticity and Some Applications. 1984.
[9] Gurtin ME, Ian Murdoch A. A continuum theory of elastic material surfaces. Archive for Rational Mechanics and Analysis 1975;57(4): 291-323.
[10] Mindlin RD, Eshel NN. On first strain-gradient theories in linear elasticity. International Journal of Solids and Structures 1968;4(1): 109-24.
[11] Fleck NA, Hutchinson JW. A reformulation of strain gradient plasticity. Journal of the Mechanics and Physics of Solids 2001;49(10): 2245-71.
[12] Yang F, Chong ACM, Lam DCC, Tong P. Couple stress based strain gradient theory for elasticity. International Journal of Solids and Structures 2002;39(10): 2731-43.
[13] Lam DCC, Yang F, Chong ACM, Wang J, Tong P. Experiments and theory in strain gradient elasticity. Journal of the Mechanics and Physics of Solids 2003;51(8): 1477-508.
[14] Lim CW, Zhang G, Reddy JN. A higher-order nonlocal elasticity and strain gradient theory and its applications in wave propagation. Journal of the Mechanics and Physics of Solids 2015;78: 298-313.
[15] Arshid E, Amir S, Loghman A. Static and dynamic analyses of FG-GNPs reinforced porous nanocomposite annular micro-plates based on MSGT. International Journal of Mechanical Sciences 2020;180: 105656.
[16] Karami B, Shahsavari D, Janghorban M. Wave propagation analysis in functionally graded (FG) nanoplates under in-plane magnetic field based on nonlocal strain gradient theory and four variable refined plate theory. Mechanics of Advanced Materials and Structures 2018;25(12): 1047-57.
[17] Do DTT, Phan D-H, Nguyen NV. A size-dependent buckling and dynamic stability performance of graphene-reinforced cellular functionally graded microplates. European Journal of Mechanics - A/Solids 2024;106: 105322.
[18] Zhou Y, Huang K. Static and dynamic stabilities of modified gradient elastic Kirchhoff–Love plates. European Journal of Mechanics - A/Solids 2024;108: 105426.
[19] Weng L, Xu F, Chen X. Three-dimensional analysis of thermoelastic damping in couple stress-based rectangular plates with nonlocal dual-phase-lag heat conduction. European Journal of Mechanics - A/Solids 2024;105: 105223.
[20] Nobili A. Asymptotically consistent size-dependent plate models based on the couple-stress theory with micro-inertia. European Journal of Mechanics - A/Solids 2021;89: 104316.
[21] Wang X, Kumar A. Size-Dependent Frequency Analysis of Higher-Order Microplates with FGP Core and Polymeric CNTRC Faces Considering Piezoelectricity. International Journal of Structural Stability and Dynamics 2023;24(15): 2450169.
[22] Zhang W, Zhang B, Shen H, Jin S, Wang Y. Size-Dependent Rigid–Flexible Coupling Dynamics of Functionally Graded Rotating Moderately Thick Microplates. International Journal of Structural Stability and Dynamics 2023;23(15): 2350169.
[23] Babaei H, Zavari S, Kaveh A, Arshid E, Civalek Ö. Dynamic Response of Advanced Lightweight Porous Plates Integrated with Nanocomposite Face Sheets Resting on Elastic Substrate. International Journal of Structural Stability and Dynamics 2024: 2550132.

[24] Ali BM, Batoo KM, Hussain S, Hussain W, Khazaal WM, Mohammed BA, et al. Scale-Dependent Generalized Thermoelastic Damping in Vibrations of Small-Sized Rectangular Plate Resonators by Considering Three-Dimensional Heat Conduction. International Journal of Structural Stability and Dynamics 2023;24(20): 2450222.

[25] Li W, Huang G. Scale-Dependent MSG Formulations for Vibrational Study of Honeycomb Microplates Covered by Piezoelectric Nanocomposite Patches. International Journal of Structural Stability and Dynamics 2023;24(19): 2450212.

[26] Saffari PR, Thongchom C, Saffari PR, Lawongkerd J, Keawsawasvong S, Senjuntichai T. Free Vibration of Thermally Loaded FG-GPLRC Nanoplates Integrated with Magneto-Electro-Elastic Layers in Contact with Fluid. International Journal of Structural Stability and Dynamics 2024: 2550113.

[27] Hosseini SMH, Tadi Beni Y, Kiani Y. Vibration Analysis of Rotating Annular Flexoelectric Microplate. International Journal of Structural Stability and Dynamics 2024: 2550126.

[28] Guo H, Cao S, Yang T, Chen Y. Vibration of laminated composite quadrilateral plates reinforced with graphene nanoplatelets using the element-free IMLS-Ritz method. International Journal of Mechanical Sciences 2018;142-143: 610-21.

[29] Karami G, Malekzadeh P. An efficient differential quadrature methodology for free vibration analysis of arbitrary straight-sided quadrilateral thin plates. Journal of Sound and Vibration 2003;263(2): 415-42.

[30] Karami G, Malekzadeh P. Static and stability analyses of arbitrary straight-sided quadrilateral thin plates by DQM. International Journal of Solids and Structures 2002;39(19): 4927-47.

[31] Kumar A, Singha MK, Tiwari V. Nonlinear bending and vibration analyses of quadrilateral composite plates. Thin-Walled Structures 2017;113: 170-80.

[32] Pasha Zanussi V, Shahverdi H, Khalafi V, Navardi MM. Nonlinear flutter analysis of quadrilateral plates consisting of functionally graded carbon nanotubes reinforced composites using Isogeometric Analysis. Thin-Walled Structures 2024;198: 111701.

[33] Mirzaei M, Ramezanghorbani F. On the Vibration Characteristics of Graphene Platelet Reinforced Composite Super-elliptical Plates via Chebyshev-Ritz Method. Engineering Analysis with Boundary Elements 2023;151: 275-86.

[34] Reddy JN. Microstructure-dependent couple stress theories of functionally graded beams. Journal of the Mechanics and Physics of Solids 2011;59(11): 2382-99.

[35] Reddy JN, Kim J. A nonlinear modified couple stress-based third-order theory of functionally graded plates. Composite Structures 2012;94(3): 1128-43.

[36] Reddy JN, Berry J. Nonlinear theories of axisymmetric bending of functionally graded circular plates with modified couple stress. Composite Structures 2012;94(12): 3664-68.

[37] Reddy JN, Romanoff J, Loya JA. Nonlinear finite element analysis of functionally graded circular plates with modified couple stress theory. European Journal of Mechanics - A/Solids 2016;56: 92-104.

[38] Nguyen XT, Hoang-Le M, Khatir S, Tran MT, Le TC. A New Modified Couple Stress Finite Element Model for Buckling Analysis of Laminated CNTs-Reinforced Composite Microplate. International Journal of Structural Stability and Dynamics 2024: 2650117.

[39] Le TC, Hoang-Le M, Ferreira AJM, Abdel Wahab M. Small size-effect isogeometric analysis for linear and nonlinear responses of porous metal foam microplate. Composite Structures 2022;285: 115189.

[40] Le TC, Le MH, Linh-Nguyen TT, Luong VH, Khatir S, Tran MT, et al. A Nonlocal Numerical Solution Based on Carrera Unified Formulation for Static and Free Vibration Analysis of Laminated Composite Nanoplate. International Journal of Structural Stability and Dynamics 2024;25(06): 2550060.

[41] Nguyen NV, Phan D-H. Assessment of dynamic instability of thin nanoplates considering size and surface energy effects. Engineering Analysis with Boundary Elements 2023;155: 861-72.

[42] Malekzadeh P, Setoodeh AR, Alibeygi Beni A. Small scale effect on the free vibration of orthotropic arbitrary straight-sided quadrilateral nanoplates. Composite Structures 2011;93(7): 1631-39.

[43] Huang LY, Han Q, Liang YJ. Calibration of nonlocal scale effect parameter for bending single-layered graphene sheet under molecular dynamics. Nano 2012;07(05): 1250033.

[44] Shenas AG, Malekzadeh P. Free vibration of functionally graded quadrilateral microplates in thermal

environment. Thin-Walled Structures 2016;106: 294-315.
[45] Babu B, Patel BP. Analytical solution for strain gradient elastic Kirchhoff rectangular plates under transverse static loading. European Journal of Mechanics - A/Solids 2019;73: 101-11.
[46] Shokravi M, Jalili N. Thermal dynamic buckling of temperature-dependent sandwich nanocomposite quadrilateral microplates using visco-higher order nonlocal strain gradient theory. Journal of Thermal Stresses 2019;42(4): 506-25.
[47] Zhang B, Li H, Kong L, Zhang X, Feng Z. Strain gradient differential quadrature finite element for moderately thick micro-plates. International Journal for Numerical Methods in Engineering 2020;121(24): 5600-46.
[48] Karamanli A. Transient vibration analysis of strain gradient multi-directional functionally graded microplates under a moving concentrated load. Composite Structures 2023;308: 116678.
[49] Emdadi M, Mohammadimehr M, Bargozini F. Vibration of a Nanocomposite Annular Sandwich Microplate Based on HSDT Using DQM. Multiscale Science and Engineering 2023;5(3): 180-94.
[50] Mao Y-H, Shang Y, Cen S, Li C-F. An efficient 3-node triangular plate element for static and dynamic analyses of microplates based on modified couple stress theory with micro-inertia. Engineering with Computers 2023;39(5): 3061-84.
[51] Mao Y-H, Shang Y, Wang Y-D. Non-conforming Trefftz finite element implementation of orthotropic Kirchhoff plate model based on consistent couple stress theory. Acta Mechanica 2023;234: 1857–87.
[52] Nuhu AA, Safaei B. A comprehensive review on the vibration analyses of small-scaled plate-based structures by utilizing the nonclassical continuum elasticity theories. Thin-Walled Structures 2022;179: 109622.
[53] Nuhu AA, Safaei B. On the Advances of Computational Nonclassical Continuum Theories of Elasticity for Bending Analyses of Small-Sized Plate-Based Structures: A Review. Archives of Computational Methods in Engineering 2023;30(5): 2959-3029.
[54] Shimpi RP. Refined Plate Theory and Its Variants. AIAA Journal 2002;40(1): 137-46.
[55] Alshenawy R, Safaei B, Sahmani S, Elmoghazy Y, Al-Alwan A, Nuwairan MA. Buckling mode transition in nonlinear strain gradient-based stability behavior of axial-thermal-electrical loaded FG piezoelectric cylindrical panels at microscale. Engineering Analysis with Boundary Elements 2022;141: 36-64.
[56] Niiranen J, Khakalo S, Balobanov V, Niemi AH. Variational formulation and isogeometric analysis for fourth-order boundary value problems of gradient-elastic bar and plane strain/stress problems. Computer Methods in Applied Mechanics and Engineering 2016;308: 182-211.
[57] Karamanli A, Vo TP, Civalek O. Higher order finite element models for transient analysis of strain gradient functionally graded microplates. European Journal of Mechanics - A/Solids 2023;99: 104933.
[58] Nguyen XT, Hoang-Le M, Khatir S, Tran MT, Cuong-Le T. A new modified couple stress finite element model for buckling analysis of laminated CNTs reinforced composite microplate. International Journal of Structural Stability and Dynamics 2024.
[59] Pedgaonkar A, Darrall BT, Dargush GF. Mixed displacement and couple stress finite element method for anisotropic centrosymmetric materials. European Journal of Mechanics - A/Solids 2021;85: 104074.
[60] Wu C-P, Lu Y-A. A Hermite-Family C1 Finite Layer Method for the Three-Dimensional Free Vibration Analysis of Exponentially Graded Piezoelectric Microplates Based on the Consistent Couple Stress Theory. International Journal of Structural Stability and Dynamics 2022;23(04): 2350044.
[61] Dargush GF. Boundary element method for three-dimensional couple stress elastostatic analysis. European Journal of Mechanics - A/Solids 2025;111: 105532.
[62] Hou D, Wang L, Yan J, Liew KM. Vibration analysis of a strain gradient plate model via a mesh-free moving Kriging Interpolation Method. Engineering Analysis with Boundary Elements 2022;135: 156-66.
[63] Atif Shahzad M, Sahmani S, Safaei B. Nonlocal couple stress-based meshless collocation model for nonlinear dynamic performance of microbeam-type piezoelectric energy harvesters. European Journal of Mechanics - A/Solids 2023;101: 105059.
[64] Saitta S, Luciano R, Vescovini R, Fantuzzi N, Fabbrocino F. Optimization of a Radial Point Interpolation Meshless strategy for strain gradient nanoplates. Engineering Analysis with Boundary Elements 2022;140: 70-78.

[65] Yan CA, Vescovini R, Fantuzzi N. A neural network-based approach for bending analysis of strain gradient nanoplates. Engineering Analysis with Boundary Elements 2023;146: 517-30.

[66] Zhang R, Cheng J, Chen T, Zhong H. A weak form quadrature element formulation of geometrically exact beams with strain gradient elasticity. European Journal of Mechanics - A/Solids 2023;99: 104912.

[67] Shang Y, Mao Y-H, Cen S, Li C-F. Generalized conforming Trefftz element for size-dependent analysis of thin microplates based on the modified couple stress theory. Engineering Analysis with Boundary Elements 2021;125: 46-58.

[68] Shang Y, Deng Z, Cen S, Li C-F. Penalty hexahedral element formulation for flexoelectric solids based on consistent couple stress theory. International Journal for Numerical Methods in Engineering 2024;125(1): e7366.

[69] Lei J, Sun Y, Wang L. Static and dynamic analysis of couple-stress elastic structures by using peridynamic differential operator. Engineering Analysis with Boundary Elements 2023;156: 20-33.

[70] Zhang B, Li H, Kong L, Zhang X, Feng Z. Variational formulation and differential quadrature finite element for freely vibrating strain gradient Kirchhoff plates. ZAMM - Journal of Applied Mathematics and Mechanics / Zeitschrift für Angewandte Mathematik und Mechanik 2021;101(6): e202000046.

[71] Zhang B, Li H, Kong L, Shen H, Zhang X. Size-dependent vibration and stability of moderately thick functionally graded micro-plates using a differential quadrature-based geometric mapping scheme. Engineering Analysis with Boundary Elements 2019;108: 339-65.

[72] Zhang B, Li H, Liu J, Shen H, Zhang X. Surface energy-enriched gradient elastic Kirchhoff plate model and a novel weak-form solution scheme. European Journal of Mechanics - A/Solids 2021;85: 104118.

[73] Duan Y, Zhang B, Zhang X, Zhang L, Shen H. Accurate mechanical buckling analysis of couple stress-based skew thick microplates. Aerospace Science and Technology 2023;132: 108056.

[74] Duan Y, Zhang B, Li X, Zhang X, Shen H. Size-Dependent Elastic Buckling of Two-Variable Refined Microplates Embedded in Elastic Medium. International Journal of Applied Mechanics 2022;14(04): 2250039.

[75] Zhang B, Li H, Kong L, Zhang X, Shen H. Strain gradient differential quadrature Kirchhoff plate finite element with the C2 partial compatibility. European Journal of Mechanics - A/Solids 2020;80: 103879.

[76] Fan H, Huang D, Wang G. Quadrilateral-area-coordinate-based numerical manifold method accommodating static and dynamic analysis. Engineering Analysis with Boundary Elements 2022;134: 315-40.

[77] Shang Y, Liu Y-D, Liu S-X. Trefftz-unsymmetric finite element for bending analysis of orthotropic plates. Engineering with Computers 2022;38(2): 1065-79.

[78] Thai H-T, Kim S-E. A size-dependent functionally graded Reddy plate model based on a modified couple stress theory. Composites Part B: Engineering 2013;45(1): 1636-45.

[79] Nguyen HX, Nguyen TN, Abdel-Wahab M, Bordas SPA, Nguyen-Xuan H, Vo TP. A refined quasi-3D isogeometric analysis for functionally graded microplates based on the modified couple stress theory. Computer Methods in Applied Mechanics and Engineering 2017;313: 904-40.

[80] Liew KM, Xiang Y, Kitipornchai S, Wang CM. Vibration Of Thick Skew Plates Based On Mindlin Shear Deformation Plate Theory. Journal of Sound and Vibration 1993;168(1): 39-69.

[81] Kitipornchai S, Xiang Y, Liew KM, Lim MK. A global approach for vibration of thick trapezoidal plates. Computers & Structures 1994;53(1): 83-92.

[82] Xiang Y, Liew KM, Kitipornchai S. Transverse Vibration of Thick Annular Sector Plates. Journal of Engineering Mechanics 1993;119(8): 1579-99.

[83] Huang CH, Hsu CH, Lin YK. Experimental and numerical investigations for the free vibration of cantilever trapezoidal plates. Journal of the Chinese Institute of Engineers 2006;29(5): 863-72.

[84] Pierre C. Mode localization and eigenvalue loci veering phenomena in disordered structures. Journal of Sound and Vibration 1988;126(3): 485-502.

[85] Dai G-Z, Wu Y-C, Ma C-C. A novel solution for dynamic behaviors of multi-span bridge plates. International Journal of Mechanical Sciences 2025;285: 109798.

[86] Deng T, Zhang B, Liu J, Shen H, Zhang X. Vibration frequency and mode localization characteristics of strain gradient variable-thickness microplates. Thin-Walled Structures 2024;199: 111779.